AGU PUBLICATIONS

Water Resources Research

RESEARCH ARTICLE
10.1002/2014WR016106

Key Points:
- Reintroducing radiometric surface temperature into Penman-Monteith (PM) model
- Holistic surface moisture availability framework to constrain the PM equation
- Numerical estimation of Priestley-Taylor parameter

Correspondence to:
K. Mallick,
kaniska.mallick@gmail.com;
kaniska.mallick@list.lu

Citation:
Mallick, K., E. Boegh, I. Trebs, J. G. Alfieri, W. P. Kustas, J. H. Prueger, D. Niyogi, N. Das, D. T. Drewry, L. Hoffmann, and A. J. Jarvis (2015), Reintroducing radiometric surface temperature into the Penman-Monteith formulation, *Water Resour. Res.*, *51*, 6214–6243, doi:10.1002/2014WR016106.

Received 7 JUL 2014
Accepted 9 JUL 2015
Accepted article online 14 JUL 2015
Published online 8 AUG 2015
Corrected 27 AUG 2015

This article was corrected on 27 AUG 2015. See the end of the full text for details.

© 2015. American Geophysical Union. All Rights Reserved.

Reintroducing radiometric surface temperature into the Penman-Monteith formulation

Kaniska Mallick[1], Eva Boegh[2], Ivonne Trebs[1], Joseph G. Alfieri[3], William P. Kustas[3], John H. Prueger[4], Dev Niyogi[5], Narendra Das[6], Darren T. Drewry[6], Lucien Hoffmann[1], and Andrew J. Jarvis[7]

[1]Department of Environmental Research and Innovation, Luxembourg Institute of Science and Technology, Belvaux, Luxembourg, [2]Department of Environmental, Social and Spatial Change, Roskilde University, Roskilde, Denmark, [3]USDA-ARS, Hydrology and Remote Sensing Laboratory, Beltsville, Maryland, USA, [4]USDA-ARS, National Laboratory for Agriculture and Environment, Ames, Iowa, USA, [5]Department of Agronomy and the Department of Earth and Atmospheric and Planetary Sciences, Purdue University, West Lafayette, Indiana, USA, [6]Jet Propulsion Laboratory, California Institute of Technology, Pasadena, California, USA, [7]Lancaster Environment Centre, Lancaster University, Lancaster, UK

Abstract Here we demonstrate a novel method to physically integrate radiometric surface temperature (T_R) into the Penman-Monteith (PM) formulation for estimating the terrestrial sensible and latent heat fluxes (H and λE) in the framework of a modified Surface Temperature Initiated Closure (STIC). It combines T_R data with standard energy balance closure models for deriving a hybrid scheme that does not require parameterization of the surface (or stomatal) and aerodynamic conductances (g_S and g_B). STIC is formed by the simultaneous solution of four state equations and it uses T_R as an additional data source for retrieving the "near surface" moisture availability (M) and the Priestley-Taylor coefficient (α). The performance of STIC is tested using high-temporal resolution T_R observations collected from different international surface energy flux experiments in conjunction with corresponding net radiation (R_N), ground heat flux (G), air temperature (T_A), and relative humidity (R_H) measurements. A comparison of the STIC outputs with the eddy covariance measurements of λE and H revealed RMSDs of 7–16% and 40–74% in half-hourly λE and H estimates. These statistics were 5–13% and 10–44% in daily λE and H. The errors and uncertainties in both surface fluxes are comparable to the models that typically use land surface parameterizations for determining the unobserved components (g_S and g_B) of the surface energy balance models. However, the scheme is simpler, has the capabilities for generating spatially explicit surface energy fluxes and independent of submodels for boundary layer developments.

1. Introduction

Radiometric surface temperature (T_R) measured via thermal infrared (TIR) remote sensing provides direct information on the land surface moisture status and surface energy balance (SEB) partitioning [*Norman et al*., 1995; *Kustas and Anderson*, 2009]. It sets the boundary condition for the transfer of latent and sensible heat through soil, vegetation, and atmosphere. The Penman-Monteith (PM) equation [*Penman*, 1948; *Monteith*, 1965] is the most pragmatic method for estimating surface to air latent heat flux (λE) (or evapotranspiration, E, in mm) from terrestrial vegetation, and the intrinsic link of the PM model with T_R emanates through the first-order dependence of the physical-ecophysiological conductances on T_R, surface moisture, and radiative fluxes [*Mallick et al*., 2014]. This equation treats the vegetation canopy as a "big-leaf" and calculates λE by combining the surface energy balance equation with a conductance-based diffusion equation. The fundamental assumption in the derivation of the PM equation was the approximation of linearity of the vapor pressure versus temperature curve ($\partial e^*/\partial T$), which *Penman* [1948] considered to be the derivative of the saturation vapor pressure curve at the air temperature (T_A) [*Lascano and van Bavel*, 2007]. The underlying objective of this assumption was to eliminate T_R from the PM formulation for calculating λE. The elimination of T_R was originally motivated by the fact that observations of T_R were not available for the scales at which estimates of λE are required [*Penman*, 1948; *Monteith*, 1965].

Despite the elimination of T_R from the PM formulation, a large number of studies have demonstrated that the internal states (e.g., soil moisture and conductances) regulating λE are strongly temperature dependent

[*Monteith*, 1981; *Huband and Monteith*, 1986; *Blonquist et al*., 2009], making T_R a primary state variable of surface energy balance closures [*Norman et al*., 1995; *Anderson et al*., 1997, 2007; *Bastiaanssen et al*., 1998; *Kustas and Norman*, 1999; *Kustas and Anderson*, 2009]. Therefore, in situations where observations of T_R are available, they can provide a rich source of information that can be used to estimate the components of the surface energy balance with in the PM model framework [*Monteith*, 1981]. However, main hindrance in implementing the PM model in TIR based SEB modeling arises because there is no direct physical method to integrate T_R information into this model. Determining the aerodynamic and surface (canopy for full vegetation, stomata for single leaf) conductance terms (g_B and g_S) is also problematic when estimating the surface fluxes using the PM framework because of the lack of robust physical models expressing g_B and g_S as a function of T_R. Given that g_B and g_S are generally not measurable at scales in which the PM equation is applied, an alternative solution to this problem so far has been the adoption of locally derived semiempirical models [*Cleugh et al*., 2007; *Mu et al*., 2007, 2011], potentially degrading the predictive quality of the physically based PM model. Major drawbacks with these classes of g_B models include their vague description, empiricism, and the requirement of substantial tuning and parameterization in order to make them applicable over the intended biomes and land surface types [*Raupach and Finnigan*, 1995; *Liu et al*., 2007; *van der Tol et al*., 2009; *van der Kwast et al*., 2009; *Ershadi et al*., 2014]. In addition, these parameterizations are not stationary due to the dynamics of the near surface boundary layer. For g_S, the situation is more problematic because g_S models are generally overparameterized with respect to the amount of calibration data actually available [*Beven*, 1979]. Predicting g_S over a wide range of hydrometeorological conditions introduces too many degrees of freedom in the form of an excessive number of physical and physiological parameters needed to be specified in the g_S models [*Jarvis*, 1976; *Beven*, 1979; *Ball et al*., 1987; *Dewar*, 1995; *Leuning*, 1995; *Katul et al*., 2010].

Recognizing this, and motivated by the advent of thermal remote sensing, an alternative modeling strategy for λE focussed on using T_R to solve the aerodynamic equation of the sensible heat flux (H) and then estimate λE as a residual of the surface energy balance [*Norman et al*., 1995; *Anderson et al*., 1997, 2007; *Bastiaanssen et al*., 1998; *Kustas and Norman*, 1999; *Su*, 2002; *Colaizzi et al*., 2012]. Although some of the outdated modeling approaches [*Hall et al*., 1992; *Cleugh et al*., 2007] have perpetrated unwarranted doubts regarding the use of T_R measurements in aerodynamic transfer equations because of the existence of large differences between T_R and aerodynamic surface temperatures (T_0) [*Troufleau et al*., 1997], advanced models using the dual-source soil-canopy framework [*Norman et al*., 1995; *Anderson et al*., 1997, 2007; *Colaizzi et al*., 2012] or the inclusion of an "extra conductance" concept in the single-source framework [*Lhomme et al*., 2000; *Su*, 2002; *Boegh et al*., 2002] appeared to accommodate the effects due to the differences between T_R and T_0. One of the core objectives of these advancements was also to by-pass the complexities associated with g_S parameterization and instead to rely on the determination of g_B for developing a thermal based λE modeling framework with "intermediate complexity".

Despite making significant advancements, the single-source and dual-source models still rely on the specifications of g_B as an external input, despite it being an internal state that provides physical feedback to both λE and H. Hence, an alternative strategy is to revisit the PM equation and attempting to reintroduce T_R into the PM formulation in a way that eliminates the need to parameterize both g_B and g_S. A recent attempt by *Mallick et al*. [2014] has elaborated on such possibilities and demonstrated a T_R based 'closure' of the PM equation in a framework referred to as the Surface Temperature Initiated Closure (STIC). STIC is formed by the simultaneous solution of four state equations where both the g_B and g_S are treated as internal states and T_R information (in conjunction with meteorological and radiation variables) is used to find their analytical solutions. STIC uses T_R as an additional data source for retrieving the "near surface" moisture availability (M) and "effective" vapor pressure at the evaporating front (e_0). STIC also combines the PM framework with the advection-aridity hypothesis [*Brutsaert and Stricker*, 1979] to find an expression of the evaporative fraction (Λ) in order to obtain the system closure (for detail please see *Mallick et al*. [2014]). The results from this initial formulation were interpreted with coarse temporal resolution (8 days) data from a large number of FLUXNET [*Baldocchi et al*., 2001] eddy covariance (EC) sites. The results showed a tendency of the STIC approach to overestimate λE under extremely dry land surface conditions. We thought such overestimation to be originating from; (a) neglecting the λE versus atmospheric vapor pressure deficit hysteresis [*Zhang et al*., 2014; *Zheng et al*., 2014] in the surface moisture availability (M) retrieval framework; (b) the use of a single value of Priestley-Taylor parameter (α); and (c) also due to overlooking the effects of moisture availability into the advection-aridity hypothesis [*Brutsaert and Stricker*, 1979] that was used for finding the state

equation of Λ. These factors are crucial when modeling λE in many regions, particularly arid, semiarid, and hyper-arid landscapes. Therefore, the original framework of STIC is modified in the present study by incorporating these important effects. The objectives of this study are as follows:

1. Reintroduction of T_R into the PM formulation for estimating λE and H by deriving surface energy balance closure expressions in order to eliminate the need of exogenous submodels for both g_B and g_S, while incorporating additional modifications in the retrieval of M, α and the evaporative fraction state equation of the original STIC framework.
2. Evaluating the performance of the modified STIC framework by comparing the λE and H estimates with high-temporal resolution (half-hourly and hourly) measurements of λE and H from four different experimental sites featuring a wide range of environmental and surface variability.
3. Analyzing the errors in the STIC derived λE and H estimates by comparing the residual errors in the surface flux estimates against environmental and land surface variables.

Section 2 describes the STIC equations along with the novel part of the M and α retrieval and the derivation of the Λ state equation as an improvement of the original STIC methodology. The field experiments and data sources used to validate the results are also described in the same section. This will be followed by an evaluation of the STIC results against EC measurements (section 3). A discussion on the results, strengths, and weaknesses of the STIC methodology and potential applicability of STIC for global change research is detailed at the end.

2. Description of STIC

STIC is based on finding an analytical solution of the surface and atmospheric conductances to obtain "closure" of the Penman-Monteith (PM) equation by integrating the radiometric surface temperature into the PM equation. A conceptual framework of STIC is given in Figure 1. It is a single-source approach where g_S represents both soil and vegetation conductances when there is partial canopy cover conditions. Under the conditions of full vegetation and (or) bare surface, g_S represents the canopy conductance and (or) bare surface conductance, respectively. A detailed derivation of the STIC equations is given in *Mallick et al*. [2014].

The PM equation states [*Monteith*, 1965],

$$\lambda E = \frac{s\phi + \rho c_P g_B D_A}{s + \gamma\left(1 + \frac{g_B}{g_S}\right)} \tag{1}$$

where ρ is the density of dry air (kg m^{-3}), c_P is the specific heat of dry air (MJ kg^{-1} K^{-1}), γ is the psychrometric constant (hPa K^{-1}), s is the slope of the saturation vapor pressure versus air temperature (hPa K^{-1}), D_A is the saturation deficit of the air (hPa) at the reference level or atmospheric vapor pressure deficit, and ϕ is the net available energy (W m^{-2}). A list of symbols used in the present study is given in Table 1.

The main assumption of the PM equation is that *Monteith* [1965] applied equation (1) to a stand of vegetation assuming the canopy to exchange H and λE with the atmosphere from a theoretical surface located at the same level as the effective sink of momentum ($z_M = d + z_0$; d is displacement height; z_0 is roughness length) [*Lhomme and Montes*, 2014]. The aerodynamic conductance (g_B) is assumed to be the same for both H and λE, and g_B is calculated between z_M and the reference height (z_R), where D_A is measured [*Lhomme and Montes*, 2014]. *Monteith* [1965] also assumed the surface conductance (g_S) to be a plant factor depending on the stomatal conductance of individual leaves and foliage area (soil evaporation was neglected) and there is a similarity between the bulk stomatal conductance and integrated component stomatal conductances under dry conditions. g_S is interpreted as the effective stomatal conductance of all the leaves acting as conductances in parallel connectivity [*Lhomme and Montes*, 2014]. The whole canopy is treated a "big-leaf" located at level $d + z_0$ and with the surface conductance g_S [*Lhomme and Montes*, 2014].

The two unknowns in equation (1) are g_B and g_S. Our aim is to derive analytical expressions of both the conductances while exploiting T_R as an external input, which will automatically integrate T_R information into the PM model. Neglecting horizontal advection and energy storage, the surface energy balance equation is written as follows:

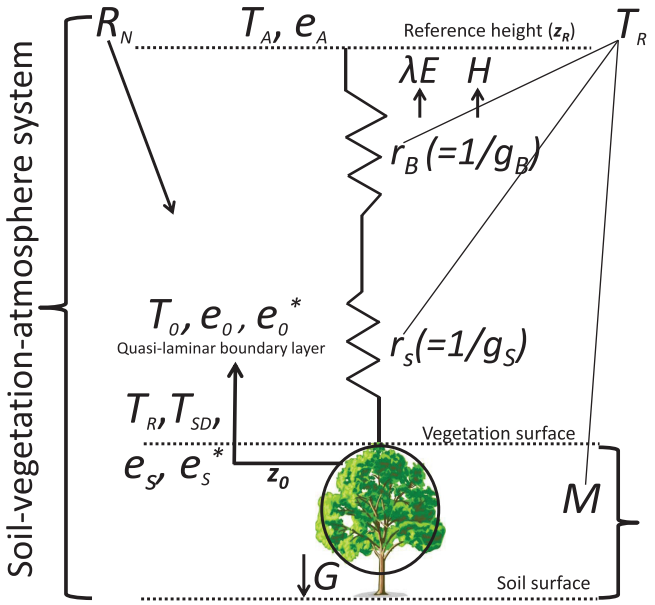

Figure 1. Schematic representation of one-dimensional description of STIC. Here r_B and r_S are the aerodynamic and surface (or canopy in case of full vegetation) resistances, g_B and g_S are the aerodynamic and surface conductances (reciprocal of resistances), e_S^* is the saturation vapor pressure of the surface, e_0^* is the saturation vapor pressure at the source-sink height, T_0 is the aerodynamic surface temperature that is responsible for transferring the sensible heat (H), e_0 is the vapor pressure at the source-sink height, e_S is the vapor pressure at the surface, z_0 is the roughness length, T_R is the radiometric surface temperature, T_{SD} is the surface dew-point temperature, M is the surface moisture availability, R_N and G are net radiation and ground heat flux, T_A and e_A are temperature and vapor pressure at the reference height (z_R), λE is the latent heat flux, H is the sensible heat flux, respectively.

$$\phi = \lambda E + H \tag{2}$$

where $\phi \cong R_N - G$, with R_N being net radiation, and G being the conductive surface heat flux or ground heat flux. All fluxes have units of W m^{-2}.

According to Figure 1, while the sensible heat flux is directed by a single aerodynamic resistance (r_B) (or $1/g_B$); the water vapor flux encounters two resistances in series, the surface resistance (r_S) (or $1/g_S$) and the aerodynamic resistance to vapor transfer ($r_S + r_B$). It is generally assumed that the aerodynamic resistance of water vapor and heat are equal, and both the fluxes are transported from the same level from near surface to the atmosphere. The sensible and latent heat flux can be expressed in the form of aerodynamic transfer equations [*Boegh et al.*, 2002; *Boegh and Soegaard*, 2004] as follows:

$$H = \rho c_P g_B (T_o - T_A) \tag{3}$$

$$\lambda E = \frac{\rho c_P}{\gamma} g_B (e_0 - e_A) = \frac{\rho c_P}{\gamma} g_S \left(e_0^* - e_0\right) \tag{4}$$

where T_A is the air temperature at the reference height (z_R), e_A is the atmospheric vapor pressure (hPa) at the level at which T_A is measured, e_0 and T_0 are the atmospheric vapor pressure and air temperature at the source/sink height [*Monteith*, 1965], or at the so-called roughness length (z_0), where wind speed is zero. They represent the vapor pressure and temperature of the quasi-laminar boundary layer in the immediate vicinity of the surface level (Figure 1), and T_0 can be obtained by extrapolating the logarithmic profile of T_A down to z_0 [*Troufleau et al.*, 1997]. e_0^* is the saturation vapor pressure at the evaporating front (hPa). Water vapor transfer occurs from within the vegetation (transpiration) and from the immediate vicinity of the vegetation (interception evaporation) and soil surface (soil evaporation). The stomatal cavities are assumed to be saturated with respect to water vapor, hence, it is expected that e_0^* of dense canopies can always be estimated from the radiometric surface temperature (T_R). For sparse vegetation, the T_R signal is a mixture of both vegetation and soil, and the estimates of e_0^* carry the mixed signal of both the canopy and soil. For extremely dry bare soil, the evaporating front may be located slightly below the dry surface layer and expressing e_0^* as a function of T_R can lead to errors. Given the potential of T_R to capture the signals of both surface and subsurface wetness [*Anderson et al.*, 2008; *Kustas and Anderson*, 2009], e_0^* is estimated from T_R in the present case.

By combining equations (2)–(4) and solving for g_B, we get

$$g_B = \frac{\phi}{\rho c_P \left[(T_o - T_A) + \left(\frac{e_0 - e_A}{\gamma} \right) \right]} \tag{5}$$

Combining the aerodynamic λE expressions of equation (4) and solving for g_S, we can express g_S in terms of g_B, e_0^*, e_0, and e_A.

Table 1. Table of Symbols and Their Description Used in the Study

Symbol	Description
λ	Latent heat of vaporization of water (J kg^{-1} K^{-1})
λE	Evaporation (evaporation + transpiration) as latent heat flux (W m^{-2})
H	Sensible heat flux (W m^{-2})
R_N	Net radiation (W m^{-2})
G	Ground heat flux (W m^{-2})
ϕ	Net available energy (W m^{-2})
E	Evapotranspiration (evaporation + transpiration) as depth of water (mm)
λE^*	Potential evaporation as flux (W m^{-2})
λE_W	Wet environment evaporation as flux (W m^{-2})
λE_P^*	Potential evaporation as flux (W m^{-2}) according to Penman
λE_{PM}^*	Potential evaporation as flux (W m^{-2}) according to Penman-Monteith
λE_{PT}^*	Potential evaporation as flux (W m^{-2}) according to Priestley-Taylor
E^*	Potential evaporation as depth of water (mm)
E_P^*	Potential evaporation as depth of water (mm) according to Penman
E_{PM}^*	Potential evaporation as depth of water (mm) according to Penman-Monteith
E_{PT}^*	Potential evaporation as depth of water (mm) according to Priestley-Taylor
E_W	Wet environment evaporation as depth of water (mm)
g_B	Boundary layer conductance (m s^{-1})
g_S	Stomatal/surface conductance (m s^{-1})
g_{Smax}	Maximum stomatal/surface conductance (m s^{-1}) (= g_S/M)
M	Surface moisture availability (0–1)
T_A	Air temperature (°C)
T_D	Dewpoint temperature (°C)
T_R	Radiometric surface temperature (°C)
T_{SD}	Surface dewpoint temperature (°C)
T_0	Aerodynamic surface temperature (°C)
R_H	Relative humidity (%)
e_A	Atmospheric vapor pressure (hPa) at the level of T_A measurement
e_0	Atmospheric vapor pressure (hPa) at the source-sink height
D_A	Atmospheric vapor pressure deficit (hPa) at the level of T_A measurement
e_S	"Effective" vapor pressure of evaporating front near the surface (hPa)
e_S^*	Saturation vapor pressure of surface (hPa)
e_0^*	Saturation vapor pressure (hPa) at the source-sink height
S	Slope of saturation vapor pressure versus temperature curve (hPa K^{-1}) (estimated at T_A)
s_1	Slope of the saturation vapor pressure and temperature between ($T_{SD} - T_D$) versus ($e_S - e_A$) (approximated at T_D) (hPa K^{-1})
s_2	Slope of the saturation vapor pressure and temperature between ($T_R - T_D$) versus ($e_S^* - e_A$) (hPa K^{-1})
s_3	Slope of the saturation vapor pressure and temperature between ($T_R - T_{SD}$) versus ($e_S^* - e_S$) (approximated at T_R) (hPa K^{-1})
s_4	Slope of the saturation vapor pressure and temperature between ($T_A - T_D$) versus ($e_A^* - e_A$) (hPa K^{-1})
W_S	Wind speed (m s^{-1})
E_A	Drying power of air
z_R	Reference height (m)
z_M	Effective source-sink height of momentum (m)
z_0	Roughness length (m)
d	Displacement height (m)
γ	Psychrometric constant (hPa K^{-1})
ρ	Density of air (kg m^{-3})
c_p	Specific heat of dry air (MJ kg^{-1} K^{-1})
Λ	Evaporative fraction
β	Bowen ratio
α	Priestley-Taylor parameter

$$g_S = g_B \frac{(e_0 - e_A)}{(e_0^* - e_0)} \tag{6}$$

While deriving expressions for g_B and g_S, two more unknown variables are introduced (e_0 and T_0), thus there are two equations and four unknowns. Therefore, two more equations are needed to close the system of equations.

2.1. Expression for T_0

An expression for T_0 is derived from the Bowen ratio (β) [*Bowen*, 1926] and evaporative fraction (Λ) [*Shuttleworth et al*., 1989] equation as described in *Mallick et al*. [2014].

$$T_o = T_A + \left(\frac{e_0 - e_A}{\gamma}\right)\left(\frac{1-\Lambda}{\Lambda}\right) \tag{7}$$

This expression for T_0 introduces another new variable (Λ); therefore, one more equation that describes the dependence of Λ on the conductances (g_B and g_S) is needed to close the system of equations. Section 2.2 describes the derivation of Λ expression while section 2.3 describes the derivation of e_0.

2.2. Derivation of Λ

In order to express Λ in terms of g_B and g_S, we had adopted the advection-aridity hypothesis [*Brutsaert and Stricker*, 1979] and introduced a modification. Although the advection-aridity hypothesis leads to an assumed link between g_B and T_R, the effects of surface moisture was not explicit in the advection-aridity equation. Present study has implemented a moisture constraint in the original advection-aridity hypothesis for deriving an expression of Λ. Deriving the expression for Λ is one of the key novelties of the STIC framework and the novel part of the derivation is described below. The logic of using the advection-aridity hypothesis for finding an expression of Λ is briefly described in Appendix A (for details see *Mallick et al.* [2014)]).

A modified form of the original advection-aridity hypothesis (equation (A2) in Appendix A) is written as follows:

$$E^*_{PM} = 2E^*_{PT} - E \tag{8}$$

Here E^*_{PM} is the potential evapotranspiration according to Penman-Monteith [*Monteith*, 1965] for any surface, and E^*_{PT} is the potential evapotranspiration according to Priestley-Taylor [*Priestley and Taylor*, 1972]. Dividing both sides by E we get,

$$\frac{E}{E^*_{PM}} = \frac{E}{2E^*_{PT} - E} \tag{9}$$

and dividing the numerator and denominator of the right-hand side of equation (9) by E^*_{PT} we get,

$$\frac{E}{E^*_{PM}} = \frac{\frac{E}{E^*_{PT}}}{2 - \frac{E}{E^*_{PT}}} \tag{10}$$

Again assuming the Priestley-Taylor equation for any surface is a variant of the PM potential evapotranspiration equation, we will derive an expression of E^*_{PT} for any surface.

$$E^*_{PM} = \frac{s\phi + \rho c_P g_B D_A}{s + \gamma\left(1 + \frac{g_B}{g_{Smax}}\right)} \tag{11}$$

$$= \frac{s\phi}{s + \gamma\left(1 + \frac{g_B}{g_{Smax}}\right)}\left(1 + \frac{\rho c_P g_B D_A}{s\Phi}\right)$$

$$= \frac{\alpha s\phi}{s + \gamma\left(1 + \frac{g_B}{g_{Smax}}\right)} \tag{12}$$

$$= E^*_{PT}$$

Here α is the Priestley-Taylor parameter [α =1.26 under nonlimiting moisture conditions, $\alpha = 1.7$ under water-limited condition, *Pereira*, 2004]. g_{Smax} is defined as the maximum possible g_S under the prevailing atmospheric conditions whereas g_S is limited due to the moisture availability (M) and hence $g_{Smax} = g_S/M$ [*Monteith*, 1995]. This approximation is very similar to the g_S equation of *Jarvis* [1976] and *Baldocchi et al.* [1991], who introduced multiple environmental drivers to constrain g_{Smax}. However, the main weakness of *Jarvis* [1976] expression is the assumption that the environmental variables operate independently [*Monteith*, 1995]. We assume that M is a significant controlling factor for the ratio of actual and potential evapotranspiration (or transpiration for a dry canopy), and the interactions between the land and environmental factors are substantially reflected in M. Since, *Penman* [1948] derived his equation over the open water surface and g_{Smax} over the water surface is very high [*Monteith*, 1965, 1981], g_B/g_{Smax} was assumed to be negligible. Introduction of leaf area index (L_{ai}) is not necessary in this case because L_{ai} plays role to scale up the

conductances from leaf to lumped canopy values, and we are already treating g_S as a lumped surface conductance.

Expressing ϕ as $\phi = E/\Lambda$ and expressing E^*_{PT} according to equation (12) gives the following expression of E/E^*_{PT}.

$$\frac{E}{E^*_{PT}} = \frac{\Lambda\left[s+\gamma\left(1+\frac{g_B}{g_{Smax}}\right)\right]}{\alpha s} \tag{13}$$

Now substituting E/E^*_{PT} from equation (13) into equation (10) and after some algebra we obtain the following expression:

$$\frac{E}{E^*_{PM}} = \frac{\Lambda\left[s+\gamma\left(1+\frac{g_B}{g_{Smax}}\right)\right]}{2\alpha s - \Lambda\left[s+\gamma\left(1+\frac{g_B}{g_{Smax}}\right)\right]} \tag{14}$$

According to the PM equation [*Monteith*, 1965] of actual and potential evapotranspiration,

$$\frac{E}{E^*_{PM}} = \frac{\frac{s\phi+\rho c_p g_B D_A}{s+\gamma\left(1+\frac{g_B}{g_S}\right)}}{\frac{s+\gamma\left(1+\frac{g_B}{g_{Smax}}\right)}{s\phi+\rho c_p g_B D_A}} \tag{15}$$

Combining equations (14) and (15) gives an expression for Λ in terms of the conductances:

$$\frac{s+\gamma\left(1+\frac{Mg_B}{g_S}\right)}{s+\gamma\left(1+\frac{g_B}{g_S}\right)} = \frac{\Lambda\left[s+\gamma\left(1+\frac{Mg_B}{g_S}\right)\right]}{2\alpha s - \Lambda\left[s+\gamma\left(1+\frac{Mg_B}{g_S}\right)\right]} \tag{16}$$

After some algebra the final expression of Λ is as follows:

$$\Lambda = \frac{2\alpha s}{2s + 2\gamma + \gamma\frac{g_B}{g_S}(1+M)} \tag{17}$$

2.3. Significance of Moisture Availability (M) and e_0 in STIC

Expression for e_0 requires the determination of near surface moisture availability (M). M is a unitless quantity which describes the relative dryness or wetness of the surface and controls the transition from potential to actual evaporation rate. Considering the general case of evaporation from any nonsaturated surface at a rate less than the potential, M is the ratio of the actual evaporation rate to the potential evaporation rate. Here M is assumed to be homogeneous between the surface and the evaporation front and its contribution to the surface vapor pressure (e_S) is given as follows [*Segal et al*., 1990; *Lee and Pielke*, 1992]:

$$e_s = e_A(1-M) + Me^*_s \tag{18}$$

e^*_s is the surface saturated vapor pressure expressed in T_R. For the extreme case where M equals zero, the surface is absolutely dry, e_S equals e_A, and no water vapor is transported from the surface to the atmosphere ($\lambda E = 0$). When M equals unity, it reflects a saturated evaporating surface (e.g., after a heavy rainfall event or irrigation). Given T_R serves as a direct metric for the surface moisture status [*Kustas and Anderson*, 2009], we used T_R in conjunction with T_A and relative humidity (R_H) to derive M within a physical estimation framework. The retrieval of M is already described in *Mallick et al*. [2014] (details in Appendix A), but a novel part is introduced here to account for any $\lambda E - D_A - T_R$ hysteresis [*Zhang et al*., 2014; *Zheng et al*., 2014].

Following *Venturini et al*. [2008], *Mallick et al*. [2014] adopted the retrieval of M (equation (A4)) with some modifications (see Appendix A for details). However, using equation (A4) for determining M was found to produce overestimation of λE under the conditions when hysteresis occurs between T_R, D_A, and λE, which is normally observed in many regions of the world [*Zhang et al*., 2014; *Zheng et al*., 2014; *Boegh et al*., 1999]. Hysteresis is found because the capacity of the soil and vegetation to supply moisture to the atmosphere is larger in the morning than in the afternoon [*Boegh et al*., 1999]. Hysteresis occurs due

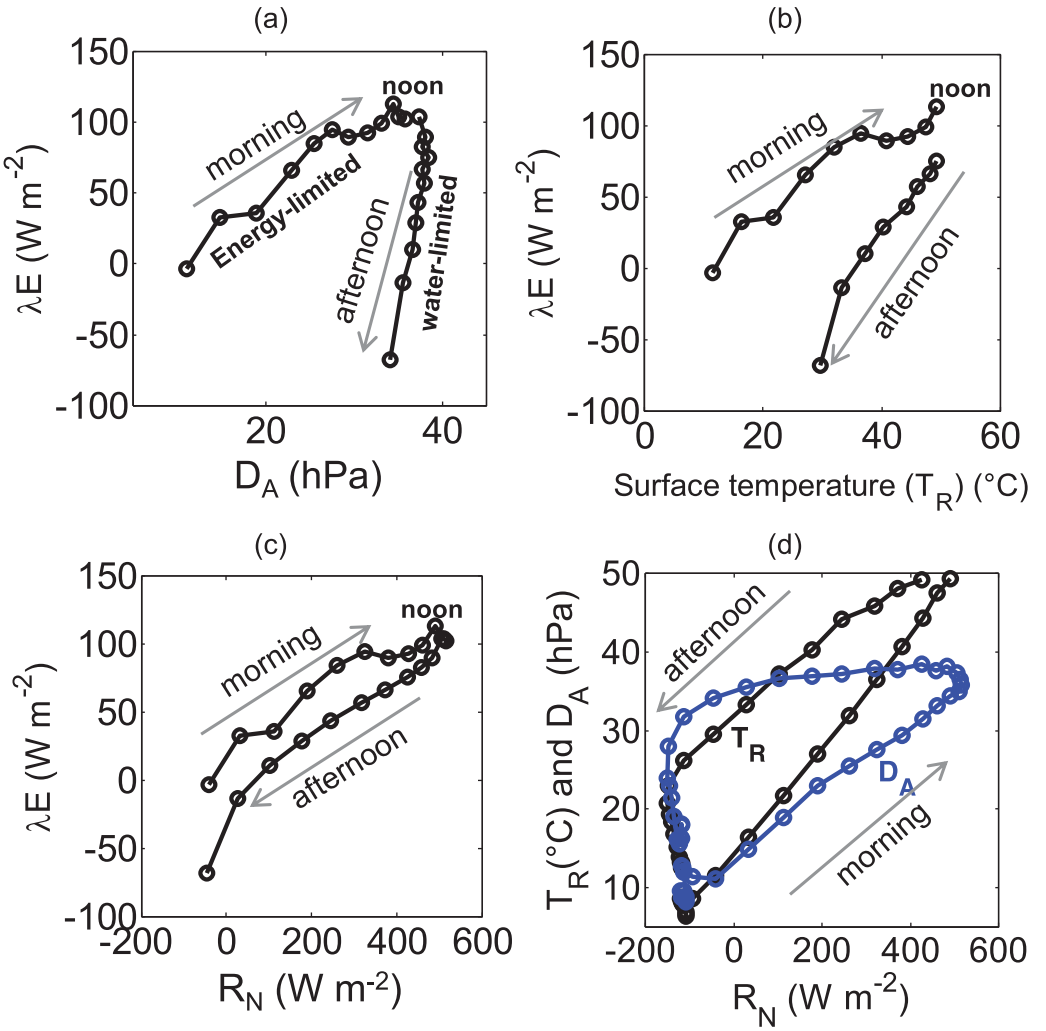

Figure 2. Measured patterns of (a) λE versus D_A, (b) λE versus T_R, (c) λE versus R_N, and (d) R_N versus T_R and D_A time series for a single representative summer day that illustrates the onset of hysteresis. The arrows indicate the energy and water limitation phases with the progression of diurnal cycle. The area covered by λE trajectories is a measure of the strength of the hysteresis [*Zhang et al.*, 2014; *Zheng et al.*, 2014]. In the arid and semiarid regions, there is both energy control and stomatal control of transpiration in the absence of water stress in the morning around 10–11 h. In the afternoon, the stomatal control of transpiration is also confounded by the water stress as described in *Boegh et al.* [1999].

to the phase difference between the diurnal cycle of R_N, T_R, and D_A (Figures 2a and 2b), which triggers the asymmetric relationship between stomatal conductance and transpiration from morning to evening [*Boegh et al.*, 1999], thus causes a rate-dependent hysteresis in the $\lambda E - D_A - T_R$ relation [*Zhang et al.*, 2014; also see *Mallick et al.*, 2013]. Hysteresis could also occur due to stomatal closure under very high D_A and low soil moisture (i.e., high T_R), which is commonly found in arid, semiarid, and hyper-arid regions [*Boegh et al.*, 1999]. Such hysteresis is associated with a clockwise looping pattern when diurnal λE is plotted against diurnal D_A and T_R (Figures 2a and 2b) [*Zhang et al.*, 2014]. When R_N and λE are perfectly in phase (for an uncoupled canopy), λE is more energy controlled (75% energy control) and both T_R as well as D_A tend to lose its control on λE. However, for a fully coupled canopy, particularly during the afternoon hours, R_N and λE are not perfectly in phase (Figure 2c) and a strong hysteresis is also observed between R_N, D_A, and T_R (Figure 2d). As shown in Figure 2d, the rate of decrease of T_R is relatively low as compared to R_N whereas D_A decreases even at a very slow rate. During this time the ecophysiology typically controls interactions between the surface to atmospheric moisture demand versus the surface moisture availability and supply. If the atmospheric moisture demand is very high (high D_A) and surface moisture is very low (high T_R), the loss of water to the atmosphere is dominated through the stored root-zone moisture, which causes a partial shutdown of the stomatal aperture [*Boegh et al.*, 1999]. As shown

in Figures 2a and 2b, the onset of hysteresis happens when the control of λE shifts from energy limitation to water limitation and the role of root-zone soil moisture becomes dominant. The hysteresis loop in the $\lambda E - T_R - D_A$ relationship occurs due to the combined effects of soil moisture changes and time lags in the environmental (e.g., R_N, T_A, D_A) and land surface drivers (T_R) that influence λE [*Zhang et al*., 2014; *Zheng et al*., 2014]. Therefore, despite D_A rises, a recession in λE is found because plants spend their stored root-zone moisture in a conservative way (Figure 2). The M retrieval method of *Venturini et al*. [2008] does not explicitly consider the complex interactions between $\lambda E - T_R - D_A$ and soil water potential-soil moisture retention phenomena during the soil moisture dry-down stages. While postulating the theory of evaporation from nonsaturated dry surfaces, *Granger and Gray* [1989] derived an expression of M that has a strong dependence on T_R, D_A, and ϕ (for the detailed derivation see *Granger and Grey* [1989]):

$$M = \frac{\gamma \lambda E}{(s\phi + \gamma E_A - s\lambda E)} \tag{19}$$

According to the aerodynamic transfer equation, λE can also be expressed as $\lambda E = f(u)(e_S - e_A)$, where $f(u)$ is the wind function that is related to g_B. E_A is generally referred to as the "drying power" of the air [*Monteith*, 1965; *Granger and Gray*, 1989] and is a product of the wind function $f(u)$ and D_A:

$$M = \frac{\gamma f(u)(e_S - e_A)}{s\phi + \gamma f(u)\left(e_A^* - e_A\right) - sf(u)(e_S - e_A)} \tag{20}$$

e_A^* is the saturation vapor pressure of air expressed in T_A. Assuming $\phi \cong E^* \cong f(u)(e_S^* - e_A)$ and cancelling $f(u)$ from both the denominator and numerator, M can be expressed as follows:

$$\begin{aligned} M &= \frac{\gamma(e_S - e_A)}{s\left(e_S^* - e_A\right) + \gamma\left(e_A^* - e_A\right) - s(e_S - e_A)} \\ &= \frac{(e_S - e_A)\gamma}{\left(e_S^* - e_S\right)s + \left(e_A^* - e_A\right)\gamma} \end{aligned} \tag{21}$$

According to the equation (21), for a dry surface, e_S is close to e_A and M approaches zero, whereas for a saturated surface $e_S \rightarrow e_S^*$ and $e_S^* \cong e_A^*$ (because surface temperature becomes very close to the ambient air temperature) and M approaches unity. At the same time under the hysteretic $\lambda E - D_A$ soil water retention conditions, equation (21) will always have an additional D_A feedback on the surface moisture availability. Expressing M in terms of the component temperatures will result in the following expression:

$$M = \frac{\gamma s_1 (T_{SD} - T_D)}{s_3 (T_R - T_{SD})s + \gamma s_4 (T_A - T_D)} \tag{22}$$

Here s_1, s_3, and s_4 are the slopes of the saturation vapor pressure and temperature between $(T_{SD} - T_D)$ versus $(e_S - e_A)$, $(T_R - T_{SD})$ versus $(e_S^* - e_S)$, and $(T_A - T_D)$ versus $(e_A^* - e_A)$ relationship. T_{SD} and T_D are the surface dewpoint temperature and air dewpoint temperature, respectively. Since T_{SD} is unknown, s_1 and s_3 are approximated at T_D and T_R. The rationale behind this approximation is described in Appendix A.

In the present study, we use the two equations (equations (A4) and (22)) for M depending on the occurrence of hysteresis. We assume equation (A4) to be the indicator of surface wetness that controls the evapotranspiration from the upper few centimetres of the surface, whereas equation (22) is assumed to be the indicator of the root-zone wetness that controls the evapotranspiration under strong hysteretic conditions between λE, R_N, T_R, and D_A. When λE is limited due to low surface wetness and high D_A, maximum λE occurs around 1–2 h before noon, after which the stomatal conductance drops down as a response to increasing D_A and water stress [*Boegh et al*., 1999]. Hysteresis was detected from the rising and falling limb of R_N, T_R, and D_A [*Zhang et al*., 2014; *Zheng et al*., 2014; *Boegh et al*., 1999] according to the two criteria, (a) if for a clear day, the R_N limb is falling after the peak R_N is reached and at the same time both the T_R and D_A limbs continue rising, those events were identified as hysteresis; (b) if both the R_N and T_R limbs are falling after the peak R_N is reached and at the same time if the D_A limb continues rising, those events were also identified as hysteresis.

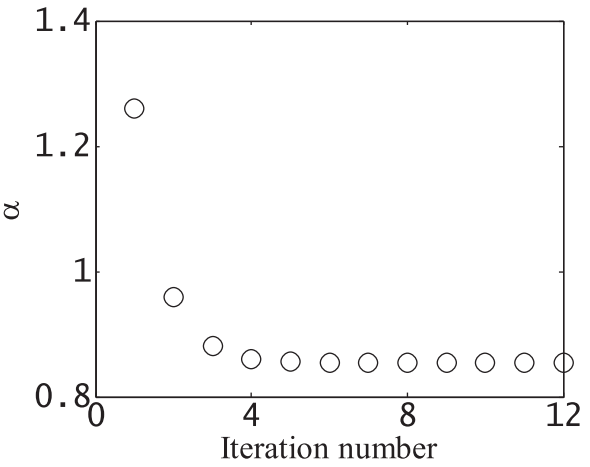

Figure 3. Convergence of the iteration method for retrieving the Priestley-Taylor coefficient (α) using equation (25). The initial values of g_B and g_S were determined with $\alpha = 1.26$. The process is then iterated by updating α in subsequent iterations with the previous estimates of g_B and g_S.

The surface moisture availability is assumed to impact both e_s and e_0. As for the e_s expression (equation (18)), M is used to estimate e_0 as follows:

$$e_0 = e_A(1-M) + Me_0^* \tag{23}$$

Although equation (23) is empirical, it is based on our expectation of how in-canopy vapor pressure behaves between extreme wet-dry surface conditions. However, in-canopy aerodynamic conductance (between soil and source/sink height and between leaves and source/sink height) is extremely difficult to model (not well developed) and empirical methods may be much better (as suggested here).

From equations (5), (6), (7), and (17), there are four unknowns (g_B, g_S, T_0, Λ), which can be solved analytically. The closure equations of STIC and estimation of the Priestley-Taylor parameter (α) are described below.

2.4. STIC Closure Equations and Estimation of α

Equation (5) (g_B), (6) (g_S), (7) (T_0), and (17) (Λ) form the four closure equations of STIC which are solved to retrieve the analytical expressions of these four unobserved variables. In the analytical expressions, the radiative (R_N, G), meteorological (T_A, R_H or e_A or T_D), land surface (T_R, M), and ecophysiological (α) variables provide the constraints to the conductances, T_0, and Λ. However, since α is still unknown, this variable is iteratively estimated. Following the equation of *Penman* [1948], the present work reports an analytical expression of the Priestley-Taylor coefficient (α) under limiting surface and environmental conditions within the framework of the PM equation [*Monteith*, 1965, 1981]. Here equation (1) is decomposed as follows to obtain a physical expression of α under limited environmental and ecohydrological conditions.

$$\lambda E = \frac{s\phi}{s+\gamma}\left[\frac{s+\gamma}{s+\gamma\left(1+\frac{g_B}{g_S}\right)} + \frac{\rho c_P g_B D_A (s+\gamma)}{s\phi\left\{s+\gamma\left(1+\frac{g_B}{g_S}\right)\right\}}\right] \tag{24}$$

$$\text{Therefore, } \alpha = \frac{s+\gamma}{s+\gamma\left(1+\frac{g_B}{g_S}\right)} + \frac{\rho c_P g_B D_A (s+\gamma)}{s\phi\left\{s+\gamma\left(1+\frac{g_B}{g_S}\right)\right\}} \tag{25}$$

After retrieving M, e_s^* (from T_R) and e_0 (from equation (23)); an initial estimate of g_B, g_S, Λ, and T_0 is obtained from the closure equations with an initial value of α (= 1.26). The process is then iterated by updating α in subsequent iterations with the previous estimates of g_B and g_S by the above mentioned physical expression (equation (25)) until a stable value of α is achieved. Repeating this process produces stable value of α within 10–12 iterations. The final α value is used in the closure equations for obtaining the final estimates of g_B, g_S, Λ, and T_0. An example of the convergence of α is shown in Figure 3. The computational sequence diagram is given in Figure 4.

3. Data Sets

Estimation of λE and H through STIC requires measurements of T_R, R_N, G, T_A, R_H, or e_A, and the dewpoint temperature of air (T_D). These radiative and meteorological variables were measured during the four different field experiments. Simultaneous micrometeorological measurements of λE and H by EC method were used to evaluate the performance of STIC. T_D was calculated from T_A and R_H according to *Buck*'s [1981] equation. Detailed descriptions of the different data sets are given below and a list of the sites is given in Table 2.

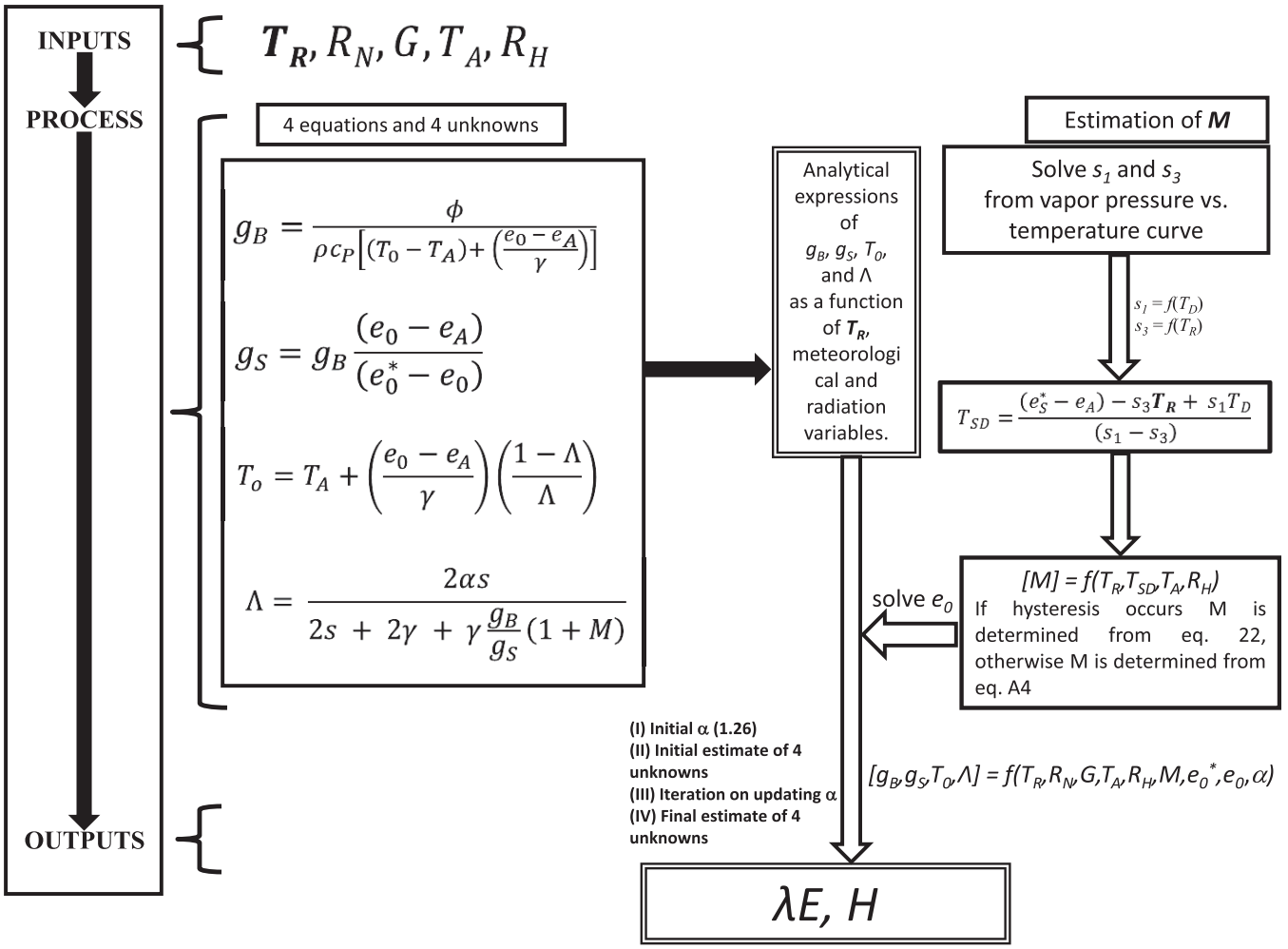

Figure 4. Computational sequence for estimating λE and H through the integration of radiometric surface temperature (T_R) into the Penman-Monteith model in the framework of STIC.

3.1. SMEX02 and SMACEX Data Set

The Soil Moisture Experiment—2002 (SMEX02) was conducted in conjugation with the Soil Moisture Atmosphere Coupling Experiment (SMACEX) [*Kustas et al*., 2005] during June and July 2002 in and around the Walnut Creek Watershed (WCW) near Ames, Iowa (41°58′N, 93°40′W). The main objectives of the experiment were to study the land-atmosphere interactions and to test and validate the thermal remote sensing based *E* algorithms over a wide spectrum of hydrothermal and vegetation conditions. The landscape was an agroecosystem with an intensive corn and soybean production region that consisted of a network of 12 meteorological and EC flux (METFLUX) towers (six soybean and six corn) (Table 2). Surface fluxes (H, λE, and G) as

Table 2. List of Sites Along With Their Characteristics Used For Testing and Verifying STIC

Experiment-Data Source	Time Period	Spatial Resolution	Temporal Resolution	Biome Type	Climate Type	Latitude	Longitude
SMEX02	2002 (DOY 171–189)	Eddy covariance footprint	30 min	Agroecosystem (corn and soybean)	Humid continental	41°58′N	93°40′W
BEAREX08	2008 (DOY 185–220)	Eddy covariance footprint	60 min	Agroecosystem (cotton)	Dry semiarid	35°11′N	102°06′W
FIFE	1987 (DOY 152–285) 1988 (DOY 132–250)	Automated meteorological station	30 min	Grassland	Temperate continental	39°N	96°88′W
SAFARI2000	2000 (DOY 59–75)	Eddy covariance footprint	30 min	Woody savanna and shrubland	Dry semiarid	20°S	22° W

well as T_R, R_N, T_A, and R_H were measured at all towers and averaged for 30 min intervals. Tower heights were maintained at approximately twice the canopy height. The intensive observation period covered a span of 18 consecutive days from day of year (DOY) 171 to 189.

3.2. BEAREX08 Data Set

The 2008 Bushland Evapotranspiration and Agricultural Remote sensing EXperiment (BEAREX08) was a multiagency field campaign near Bushland, Texas (35°11′N, 102°06′W, 1170 m elevation above MSL) to investigate and compare different field and remote sensing based approaches for measuring surface energy fluxes [*Evett et al*., 2012]. More specifically, the primary goal of BEAREX08 was to investigate the impact of meso and microscale advective processes on λE measurements from dryland and irrigated agricultural fields, and how well these impacts are captured by remote sensing and predictive modeling systems. The study area consisted of four adjacent fields (each 4.7 ha) containing irrigated and dryland cotton along with nearby bare soil, wheat stubbles, and rangeland fields using nine EC stations, three large aperture scintillometers, and three Bowen ratio systems. The data used in this study were collected in the irrigated cotton fields. Surface fluxes (H, λE, and G), T_R, R_N, T_A, and R_H were measured at 60 min intervals at all of the towers. The detailed description of the BEAREX08 field campaign can be found in *Evett et al*. [2012] while a complete discussion of the data from the four EC stations can be found in *Alfieri et al*. [2011, 2012].

3.3. FIFE Data Set

The First ISLSCP (International Satellite Land Surface Climatology Project) Field Experiment (FIFE) was a land surface atmosphere exchange experiment conducted in and around the 15 km × 15 km Konza Prairie Long Term Ecological Research (LTER) site centered at 39°N, 96°88′W near Manhattan, Kansas [*Sellers et al*., 1992]. The land cover was predominantly a grassland ecosystem. Surface data from 10 Portable Automatic Meteorological (PAM) stations were collected during three consecutive summers from 1 May 1987 to 10 November 1989. Meteorological and surface flux measurements were also conducted at multiple sites (22 sites in 1987, 10 in 1988, and 14 in 1989) [*Kanemasu et al*., 1992]. Surface flux and meteorological data collected at all the sites were averaged for each year from 1987 to 1989 (for details on averaging, data processing, and quality control methods see *Betts and Ball* [1998]). Although significant heterogeneity was found between sites [*Betts and Ball*, 1998], no attempts were made to account for land cover when averaging the data for the sites. The data are available at www.alanbetts.com/research/. Given the limited data availability for 1989, we have used the data of 1987 and 1988 in the present analysis.

3.4. SAFARI2000 Data Set

SAFARI2000 was an international science initiative in Southern Africa to investigate biosphere-atmosphere exchange processes [*Scholes et al*., 2002]. Campaign-based EC measurements of carbon dioxide, water, and energy fluxes (30 min averages) were made at four locations along a mean annual precipitation gradient in southern Africa during the SAFARI 2000 wet (growing) season campaign in the year 2000. Measurements were conducted along the Kalahari Transect and cover a gradient of average annual precipitation from 879 mm in Mongu to 365 mm in Tshane. This climate gradient is reflected by vegetation type and structure covering broadleaf evergreen forest in the north to open savanna in the south. EC instruments were installed on a permanent tower in Mongu, Zambia (879 mm of rainfall per year), as well as on a portable tower in Maun (460 mm/yr), Okwa River Crossing in Ghanzi (407 mm/yr), and Tshane (365 mm/yr), Botswana for several days at each site. As λE data of Mongu and Tshane were very noisy, we omitted these data in the present analysis. The data are available at ftp://daac.ornl.gov/data/safari2k/.

The main reasons for selecting these four experimental data sets were (a) they cover a wide range of surface and atmospheric dryness-wetness conditions, (b) data are substantially quality controlled, and (c) they were used earlier to test and validate some sophisticated thermal remote sensing based λE algorithms [*Norman et al*., 1995; *Anderson et al*., 1997, 2007, 2012; *Su*, 2002]. Another important advantage of using these data sets was the availability of high-frequency T_R measurements within the EC footprint, along with the micrometeorological and meteorological measurements. The surface energy balance data were already closed in the FIFE data sets. For the rest of the experimental data sets, the surface energy balance was closed by applying the Bowen ratio [*Bowen*, 1926] closure as described in *Chavez et al*. [2005] and later adopted by *Anderson et al*. [2007] and *Mallick et al*. [2014]. It is important to mention, for SMEX02, data from six individual corn and six individual soybean sites were combined (or concatenated) and crop wise analysis was conducted. Similarly, data from four BEAREX08 sites and data from two SAFARI2000 sites were individually

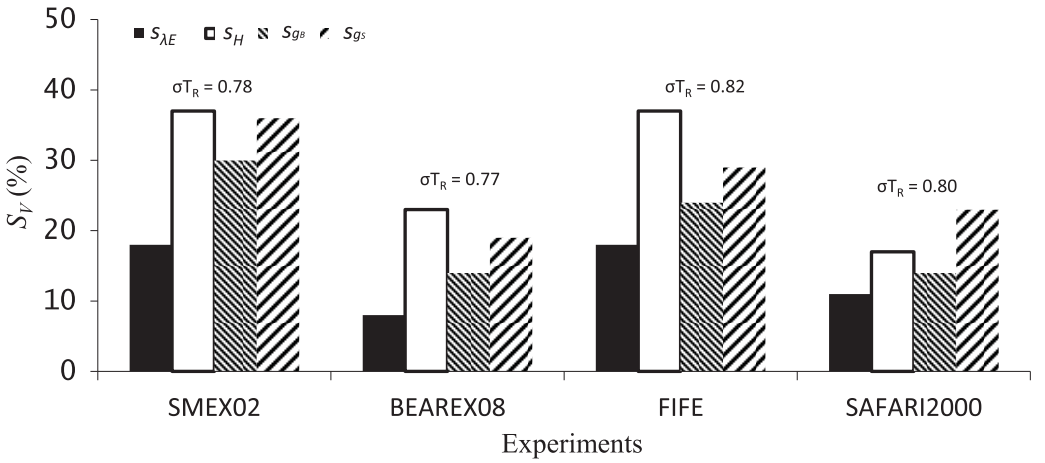

Figure 5. Sensitivity of the STIC derived fluxes (λE and H) and conductances (g_B and g_S) to random uncertainties in radiometer measured T_R (σT_R). One representative site from every experiment is chosen. The numbers of data points were 919 for SMEX02, 1488 for BEAREX08, 6624 for FIFE, and 135 for SAFARI2000. Average sensitivity of all data points is reported.

combined (or concatenated). The surface energy balance of individual EC stations was closed at first before concatenating the data. For every individual experiment, similar kind of meteorological, radiation, and surface flux measurement sensors were used in the multiple EC stations, and the sensor precision as well as accuracy was the same within the experiments.

4. Results

4.1. Sensitivity of Conductances and Surface Fluxes to T_R

The accuracy of the conductance and surface flux retrieval through STIC depends on the quality of T_R. Therefore, a sensitivity analysis of STIC was first carried out to quantify the impacts of uncertainty in T_R on g_B, g_S, λE, and H. The sensitivity analysis will indicate the accuracy that is necessary in T_R measurements to retrieve reliable surface energy fluxes. Sensitivity analyses were conducted by increasing and decreasing T_R randomly from its original value while keeping the other variables and parameters constant. This procedure was selected because the fluxes and conductances reflect an integrated effect of T_R and it shows substantial variability throughout the year. First, the base conductances and fluxes were computed using the base T_R data. Then T_R was varied randomly and a new set of conductances and fluxes were computed. The nature of the sensitivity analysis used here is similar to that of *Anderson et al*. [1997]: the absolute sensitivity (S_V) of any of the output variable (V) to $\pm X$ uncertainty in T_R was assigned as $S_V = |\ (V_{X+} - V_{X-})/V_{Xr}\ |$. S_V of 0.1 signifies 10% and 1 signifies 100%. Here V_{X+} and V_{X-} are the estimated variables when the value of T_R is increased or decreased by X and V_{Xr} is the value of the estimated variable at "true" T_R. The averaged random uncertainties of T_R were 0.78, 0.77, 0.82, and 0.80 K for SMEX02, BEAREX08, FIFE, and SAFARI2000, respectively (Figure 5). Both the fluxes and conductances were found to be significantly sensitive to the T_R uncertainties. However, the sensitivity of H among the two fluxes was higher, while the sensitivity of g_S was higher among the two conductances (Figure 5). The magnitude of average S_V varied from 14% to 30% for g_B, 19% to 36% for g_S, 8% to 18% for λE, and 17% to 37% for H, respectively (Figure 5).

4.2. Evaluation of Half-Hourly and Hourly λE and H

The performance of STIC was evaluated using the measures suggested by *Willmott* [1982]. These include the statistical analysis of root-mean-square deviation (RMSD) (both systematic, RMSD$_S$ and unsystematic or random, RMSD$_U$) (see Table 3 for the definition), mean absolute percent deviation (MAPD) and correlations coefficient (r). According to *Willmott* [1982], systematic error (RMSD$_S$) should be less than the random error (RMSD$_U$). The proportion of the total RMSD arising from systematic biases is reflected in the quantity RMSDs^2/RMSD^2 [*Willmott*, 1982].

Estimates of λE and H from STIC at half-hourly (hourly for BEAREX08) temporal resolution are compared to the measurements (Figure 6) for all the four experiments. In all four experiments, both the predicted λE and

Table 3. Quantitative Measures (Error Statistics) of the Performance of STIC for Hourly λE and H Estimates[a]

Flux	Experiment	Crop/Tower ID/yr	N	$\bar{O}$ (W m^{-2})	$\bar{P}$ (W m^{-2})	Slope	Intercept	MAPD (%)	RMSD (W m^{-2})	$RMSD_S$ (W m^{-2})	$RMSD_U$ (W m^{-2})	r
λE	SMEX02	Corn	4585	332	329	0.94	16	6	25	10	23	0.98
		Soybean	5178	233	234	1.01	−1	10	33	2	33	0.97
	BEAREX08	EC1	1488	226	223	0.94	12	14	43	12	41	0.97
		EC2	1488	212	206	0.85	26	19	56	26	50	0.95
		EC8	1488	287	268	0.94	−1	12	47	23	42	0.98
		EC9	1488	277	282	1	−4	12	47	5	47	0.98
	FIFE	1987	6624	216	236	0.90	40	16	44	22	38	0.94
		1988	6288	217	223	0.87	34	15	44	16	41	0.93
	SAFARI2000	Ghanzi	135	78	94	0.80	35	15	38	14	35	0.84
		Maun	235	114	116	0.85	53	10	39	18	25	0.92
H	SMEX02	Corn	4585	63	66	0.75	19	30	25	10	22	0.79
		Soybean	5178	65	63	0.72	16	36	33	19	27	0.88
	BEAREX08	EC1	1488	68	70	0.83	14	45	43	17	39	0.90
		EC2	1488	76	82	0.80	21	53	56	23	51	0.87
		EC8	1488	84	89	0.98	20	74	48	19	44	0.90
		EC9	1488	78	73	0.92	8	77	48	7	47	0.87
	FIFE	1987	6624	96	83	0.70	16	31	40	25	30	0.86
		1988	6288	106	99	0.79	16	30	44	17	40	0.82
	SAFARI 2000	Ghanzi	135	55	70	1.08	−11	20	38	7	37	0.92
		Maun	235	43	44	1	−12	21	39	11	39	0.90

[a]N = number of observations; $\bar{O}$ = mean observed flux; $\bar{P}$= mean predicted flux; MAPD is the percent error defined as the mean-absolute-deviation between observed (O) and predicted (P) flux divided by mean observed flux; RMSD = root-mean-square deviation = $\left[\frac{1}{N}\sum_{i=0}^{N}(P_i-O_i)^2\right]^2$; $RMSD_S$ = systematic RMSD = $\left[\frac{1}{N}\sum_{i=0}^{N}(\dot{P}_i-O_i)^2\right]^2$; $RMSD_u$ = unsystematic RMSD = $\left[\frac{1}{N}\sum_{i=0}^{N}(P_i-\dot{P}_i)^2\right]^2$; $\dot{P}_i = c + mO_i$; m and c are the slope and intercept of linear regression of P on O.

H are generally in good agreement with the observations, with reasonable correlation (r) (r range between 0.82 and 0.98) between observed and STIC fluxes. Regression statistics varied between 0.85 and 1.01 for the slope and −4 to 53 for the offset for λE (Table 3), whereas for H, these were 0.7–1 for the slope and −12 to 21 for the offset (Table 3), respectively. The scatter between the observed and predicted λE was reasonably small (Figure 6) while the comparison of H shows relatively larger scatter between the modeled and measured values. This was in particular the case for BEAREX08 and FIFE (inset of Figure 6), thus resulting in higher RMSD and MAPD for H.

Quantitative measures (error statistics) of the STIC performance at half-hourly (hourly for BEAREX08) temporal resolution are shown in Table 3. For SMEX02, λE and H derived by STIC were generally in good agreement with the observations. The difference between mean observed and predicted values of both λE and H is fairly small (2–7 W m^{-2} and −2 to −3 W m^{-2}). The relative sizes of RMSDs to RMSD for both fluxes indicate a small systematic difference. For λE the $RMSDs^2/RMSD^2$ proportion varied from 0.03% to 16% whereas for H this proportion was 16% to 33%. However, the percent errors (MAPD) in H are relatively large because the magnitude of the observed H is small. For BEAREX08, the magnitude of bias was −6 to −17 W m^{-2} for λE and 2–19 W m^{-2} for H. Both fluxes had reasonably small RMSDs values, which again indicate a small systematic difference between the observed and predicted fluxes. The ratio of $RMSDs^2/RMSD^2$ was 1–22% for λE and 2–17% for H, respectively (Table 3). For the FIFE data, the ratio of $RMSDs^2/RMSD^2$ varied between 13% and 25% for λE, whereas this ratio was 15–39% for H (Table 3). The MAPD in H was high for both BEAREX08 (45% to 77%) and FIFE (30–31%) sites. For the SAFARI2000, the MAPD of both fluxes varied from 10% to 15% and 20% to 21%, respectively (Table 3). The proportion of the systematic difference was also low for both λE (13–21%) and H (3–8%).

4.3. Evaluation of Daily and Seasonal λE and H

Hourly fluxes were aggregated into daytime totals and compared with the measured fluxes as shown in Figure 7, with associated error statistics given in Table 4. For SMEX02, STIC performed efficiently in capturing the daily λE and H patterns of both corn and soybean (Figures 7a and 7c), although there was slight underestimation of λE over corn (Figure 7b). This was also evidenced by the negative intercept of the least square regression between the observed and STIC λE (Table 4). For the BEAREX08 experiment, STIC was unable to

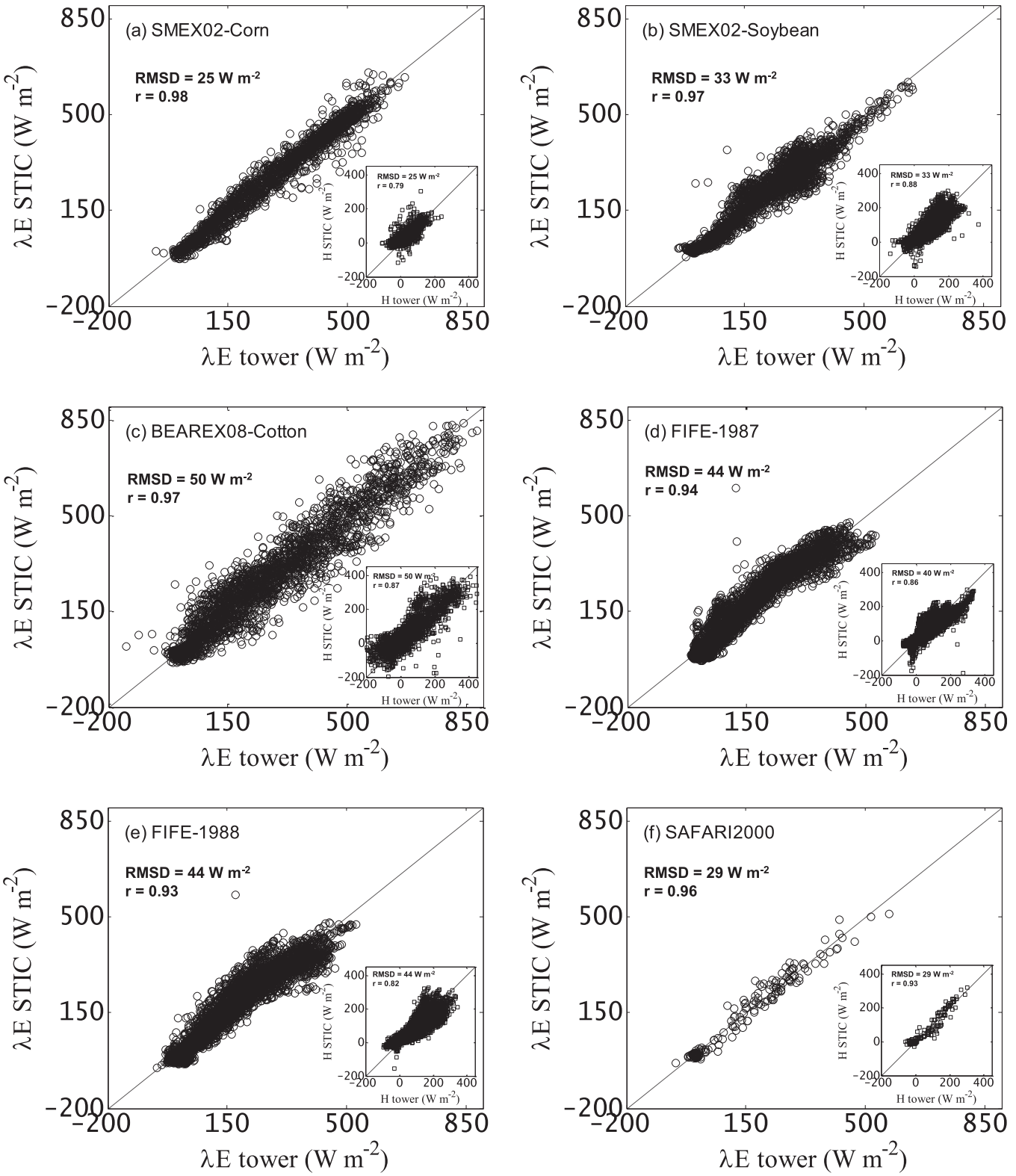

Figure 6. Comparison of measured versus STIC estimates of λE and H (inset) using hourly data of SMEX02, BEAREX08, FIFE, and SAFARI2000 experiments.

effectively capture the advective enhancement in λE that occurred during day of year (DOY) 215–217 DOY, as evidenced in Figure 7f. However, the daily λE dynamics on some of the days with minor advection from DOY 177 to 203 was fairly well captured by STIC. For the FIFE data, the scatter between observed and

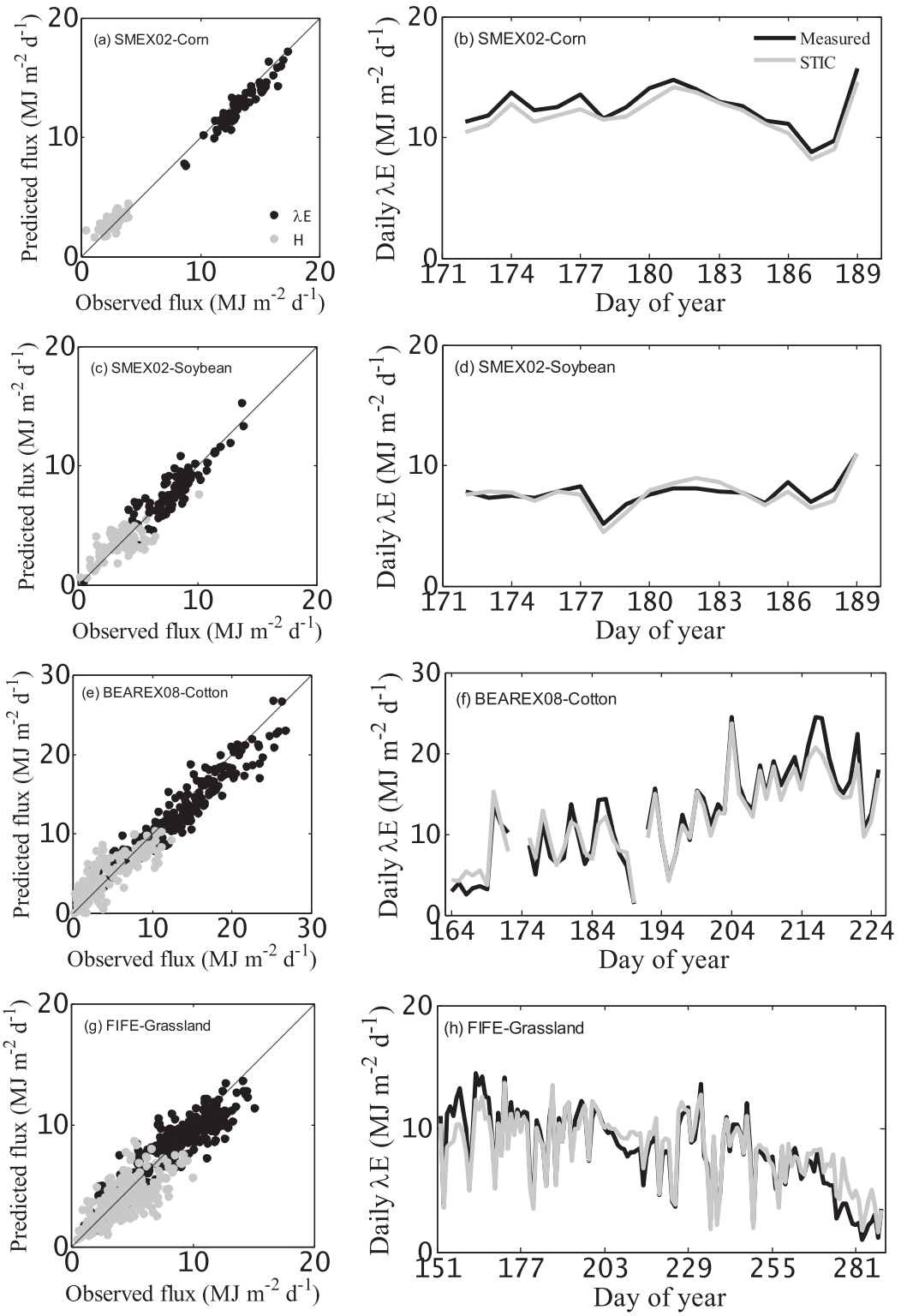

Figure 7. (a, c, e, and f) Comparison of STIC predicted daily λE (black dots) and H (gray dots) with measured flux components over the individual land cover types, integrated to daytime totals (MJ m^{-2} d^{-1}). (b, d, f, and h) Time series of daily λE observed over different crops compared with predicted λE from STIC.

estimated λE and H was relatively large as compared to the other experiments (Figure 7g). Errors in the daily step are smaller (Table 4) than for hourly fluxes due to cancellation of random errors through the course of the day. Generally, the difference between mean predicted and observed values of both λE and H varied

Table 4. Quantitative Measures (Error Statistics) of the Performance of STIC for Daily λE and H Estimates

Flux	Experiment	Land Use	N	$\bar{O}$ (MJ m^{-2} d^{-1})	$\bar{P}$ (MJ m^{-2} d^{-1})	Slope	Intercept	MAPD (%)	RMSD (MJ m^{-2} d^{-1})	$RMSD_S$ (MJ m^{-2} d^{-1})	$RMSD_U$ (MJ m^{-2} d^{-1})	r
λE	SMEX02	Corn	72	13.28	12.68	0.97	−0.14	5	0.82	0.60	0.55	0.95
		Soybean	108	8.03	8.04	0.80	1.59	9	0.98	0.33	0.90	0.83
	BEAREX08	Cotton	248	13.21	12.56	0.83	1.61	11	1.65	0.93	1.36	0.95
	FIFE	Grassland	269	8.41	8.31	0.75	2.02	13	1.34	0.76	1.10	0.90
	SAFARI2000	Woodland and shrubland	6	9.16	9.17	0.93	0.66	4	0.47	0.20	0.42	0.99
H	SMEX02	Corn	72	2.50	2.90	0.63	1.32	19	0.62	0.46	0.42	0.74
		Soybean	108	3.43	3.44	0.48	1.78	25	1.11	0.79	0.77	0.68
	BEAREX08	Cotton	248	4.08	4.58	0.67	1.85	35	1.81	1.12	1.42	0.82
	FIFE	Grassland	269	4.38	3.97	0.58	1.43	27	1.49	0.92	1.17	0.69
	SAFARI2000	Woodland and shrubland	6	4.79	4.74	1.05	−0.29	9	0.47	0.10	0.46	0.97

between 0.01 to −0.65 MJ m^{-2} and −0.40 to 0.50 MJ m^{-2} (Table 4). MAPD of the daytime λE and H values varied from 5% to 13% and from 9% to 35%, respectively (Table 4). For λE, the proportion of $RMSD_S^2/RMSD^2$ varied from 11% to 53% whereas for H this proportion ranged from 4% to 55% (Table 4). The magnitude RMSD in daytime total λE varied from 0.47 to 1.65 MJ m^{-2}, which was 5% to 16% of the observed λE (Table 4). For H, the RMSD was 0.47 to 1.81 MJ m^{-2}, which was 10 to 44% of the observed daytime H (Table 4).

The average seasonal cumulative values of λE (E, mm) for different experiments are shown in Figure 8. Since, time series observations of the individual flux sites in SMEX02 and BEAREX08 were incomplete, data from all the corn and soybean in SMEX02 and all cotton sites in BEAREX08 are averaged to produce cumulative corn E, soybean E, and cotton E, respectively. For corn there was a consistent underestimation of cumulative E to the order of 5–8% (Figure 8a) whereas for soybean there was a consistent overestimation (2–7%)

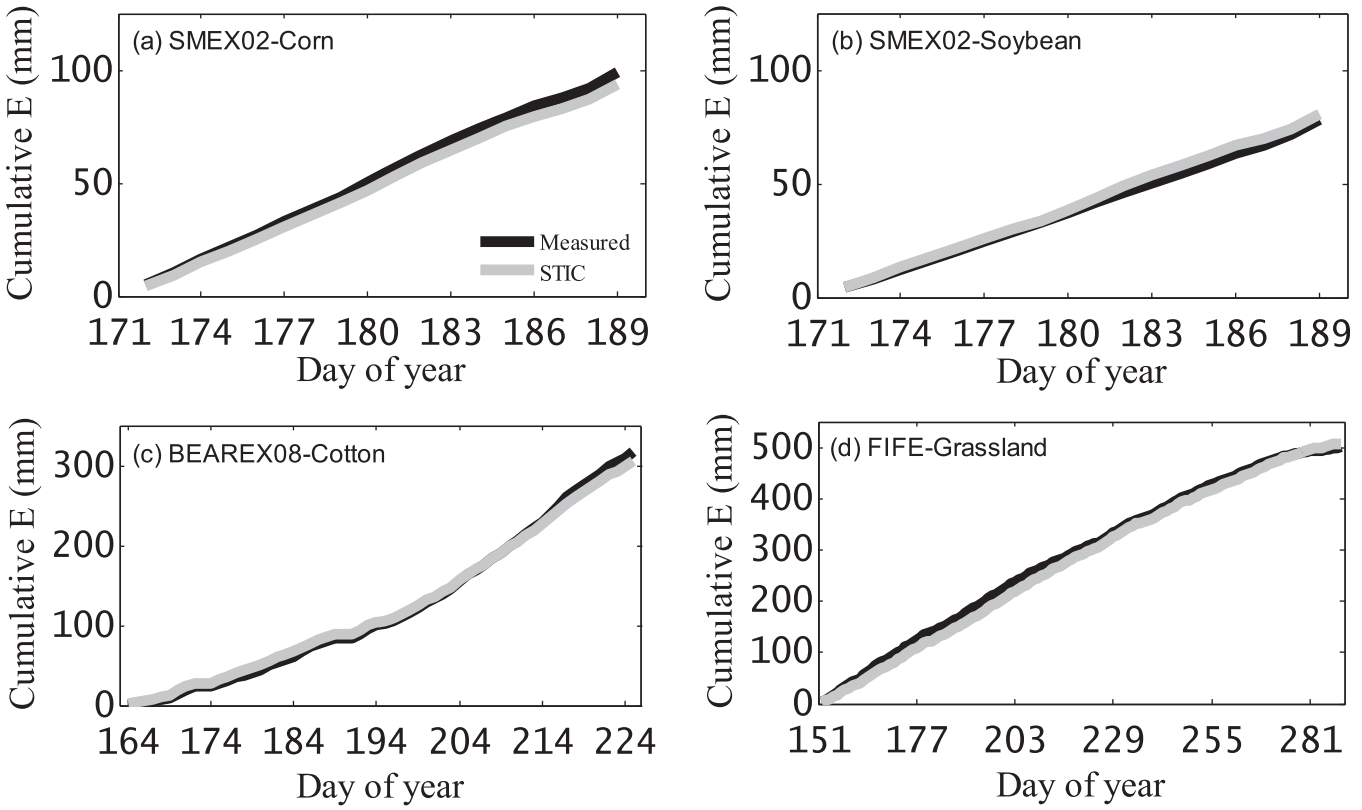

Figure 8. Cumulative modeled and measured E averaged over all the land cover types. For SMEX02 and BEAREX08, this averaging is done by combining the data of all the corn, soybean and cotton sites, respectively. For the FIFE, this averaging is done by combining the data of 1987 and 1988.

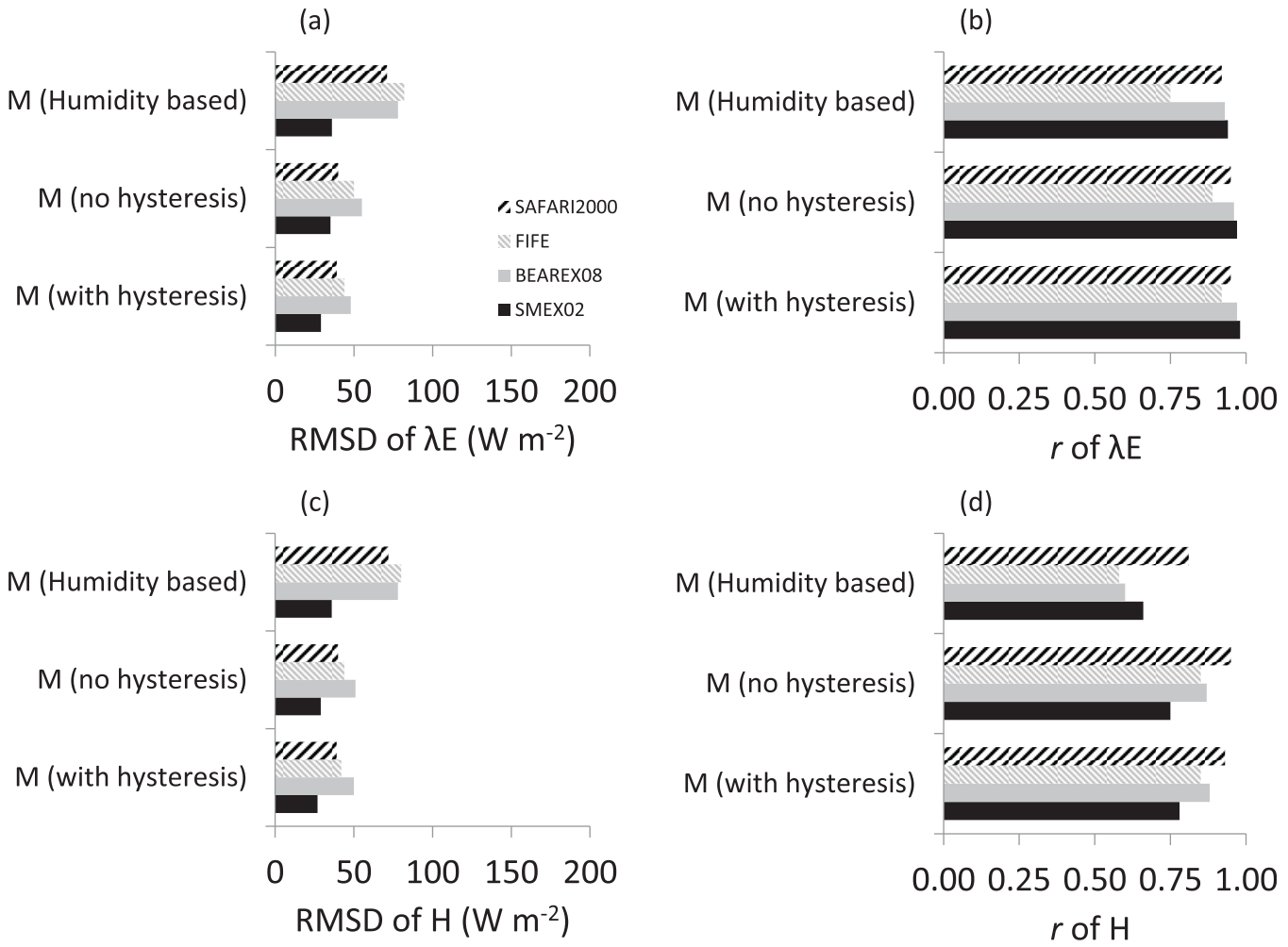

Figure 9. Impact of three different surface moisture availability (M) representations on the error statistics (RMSD and r) of (a and b) λE and (c and d) H. This shows T_R to be a stronger variable to constrain M and the surface fluxes as compared to the relative humidity (R_H). R_H-based method yielded higher RMSD and lower r as compared to T_R in all the experiments other than the SMEX02.

after DOY 180 (Figure 8b). For cotton, although there was a consistent overestimation (15–50%) of cumulative E in the initial stage (from DOY 164 to 174), but the error was reduced after DOY 174 (−4% to 10%) (Figure 8c). For the grassland of FIFE, the error in cumulative modeled E was within −18% to 1% (Figure 8d). Overall, the errors in cumulative E computed from STIC were within 2–6% of the cumulative observed E.

4.4. Impact of Moisture Availability Representation on Modeled Fluxes

An intercomparison of half-hourly (hourly for BEAREX08) λE and H estimates against different M retrieval methodologies is also conducted by comparing the statistics (RMSD and r) using two different M retrieval approaches. In those cases, M was estimated (a) without assuming any hysteresis by employing equation (A4) only and (b) by employing the air relative humidity and vapor pressure deficit (a modified PMBL method of *Mallick et al.* [2013]) (see Appendix B for modified PMBL), respectively. The results (Figure 9) indicate significant improvements in λE (RMSD improved by 19–46%; r improved by 3–23%) (Figures 9a and 9b) and H estimates (RMSD improved by 25–48%; r improved by 15–47%) (Figures 9c and 9d) for all the experiments (with the exception of SMEX02 where the RMSD improvement was not substantial) when T_R was used for constraining M in the STIC framework as compared to $R_H - D_A$ based M estimates. However, very low (for SAFARI2000) to moderate improvements (SMEX02, BEAREX08, and FIFE) were found between the T_R-based hysteretic and nonhysteretic λE (RMSD improved by 3–17% and

r improved by 0–3%) (Figures 9a and 9b) and H estimates (RMSD improved by 3–7%; r improved by 0–4%) (Figures 9c and 9d).

4.5. Error Analysis of λE and H Estimates

A residual error (ε) (= predicted flux − observed flux) analysis was conducted to quantify the impacts of biophysical, radiation, and meteorological variables on the error propagation in both λE and H estimates. BEAREX08 data were chosen for this analysis because this experiment was conducted for a relatively longer time period and covers a wide range of atmospheric turbulence, meteorological, and surface wetness conditions. The distributions of ε against different limits of biophysical, radiation, and meteorological variables are shown in box and whisker plots (Figures 10a, 10c, 10e, 10g, and 10i). The boxplots show the median and interquartile range of the ε distribution and illustrate whether the distribution of ε is symmetric or skewed for the observed ranges of different input variables that control the modeled λE. The direction of ε in H was opposite to λE (therefore the figures of residual error of H are not shown). In general, the residual λE and H errors ($\varepsilon_{\lambda E}$ and ε_H) were very weakly correlated ($r = \pm 0.04$) with the observed difference between T_R and T_A ($dT_{R\text{-}A}$) for the entire range of $dT_{R\text{-}A}$. From Figure 10a, it is evident that there was a negligible overall positive mean $\varepsilon_{\lambda E}$ when $dT_{R\text{-}A}$ increases beyond 10°C and $\varepsilon_{\lambda E}$ was only 0.3%. Figure 10b confirms that this error is systematic since the ratio of RMSDs^2/RMSD^2 for both H and λE is close to unity (100%). Both $\varepsilon_{\lambda E}$ and ε_H were weakly correlated ($r = \pm 0.22$) with wind speed (W_S) (Figure 10c) and an error of 4.5% was introduced into the flux estimates by neglecting the W_S information into the STIC framework. The systematic RMSD was higher for H than for λE for high values of W_S (Figure 10d). Overall correlation between $\varepsilon_{\lambda E}$ and D_A was also weak, to the order of 0.11. However, when D_A exceeds 40 hPa, $\varepsilon_{\lambda E}$ was positively skewed (Figures 10d and 10e) and r increased up to 0.17. The strongest relationship between $\varepsilon_{\lambda E}$ and D_A was found when D_A exceeded 40 hPa and W_S exceeded 8 m s^{-1} when approximately 72% error was introduced into the estimates of λE (results not shown). However, such conditions are rarely found and only 0.2% of the total data exhibited this atypical combination of D_A and W_S. It is also evident from Figure 10f that the ratio of RMSDs^2/RMSD^2 for λE was greatest when D_A exceeds 40 hPa. The correlation between $\varepsilon_{\lambda E}$ and T_R was weak ($r = 0.25$) (i.e., 6% error) and $\varepsilon_{\lambda E}$ distribution was positively skewed when $T_R > 45$°C (Figure 10g). As shown in Figure 10h, the proportion of systematic error was higher in λE (RMSDs^2/RMSD^2 = 0.70) compared to H (RMSDs^2/RMSD^2 = 0.35). Both the residual errors were weakly correlated with ϕ ($r = \pm 0.18$) (i.e., 3% error) as also evidenced in Figure 10i. Figure10j also brings out the fact that although the systematic errors in both H and λE were larger for the smaller values of ϕ but the magnitude of RMSDs^2/RMSD^2 are reduced at high values of ϕ (Figure 10j).

To probe the errors of the surface fluxes, we further investigated the λE RMSD in relation to the retrieved M for the BEAREX08 and FIFE experiments (Figure 11) (because of the longer durations of these two experiments as compared to the others). The analysis revealed that the majority of the RMSD in λE is originated under substantial surface dryness conditions when M was between 0 and 0.25, after which the RMSD is reduced significantly. For the BEAREX08, the RMSD in λE is reduced by 32% to 89% (from 65 W m^{-2} to 44, 25 and 5 W m^{-2} with increasing M) and for FIFE the RMSD is reduced by 48% to 75% (from 68 W m^{-2} to 35, 17 and 21 W m^{-2} with increasing M) (Figure 11).

5. Discussion

The surface flux estimates from STIC are able to capture the observed high-temporal frequency dynamics of the fluxes covering a wide range of surface and environmental conditions and provide reasonable estimates of λE (and H). Among the two surface fluxes, H was relatively more sensitive to the errors in T_R (Figure 5). Since the difference between T_R and T_A is considered to be the primary driving force of H [*van der Tol et al.*, 2009] the modeled flux estimates responded as expected due to the uncertainties in T_R. Among the two conductances, the relatively greater sensitivity of g_S toward T_R uncertainty (Figure 5) is attributed due to the high response of g_S to moisture transport in the soil-plant-atmosphere system [*Manzoni et al.*, 2013]. This could also be associated with the intrinsic link between g_S and T_R through the surface energy balance [*Campbell and Norman*, 1998]. Overall, the high sensitivity of the fluxes and conductances to T_R stresses the need for high-quality T_R data in surface energy balance modeling. It is also important to mention that uncertainties in T_R will also amplify the uncertainties both in R_N and G, but to a small extent (to the order of 2–6%

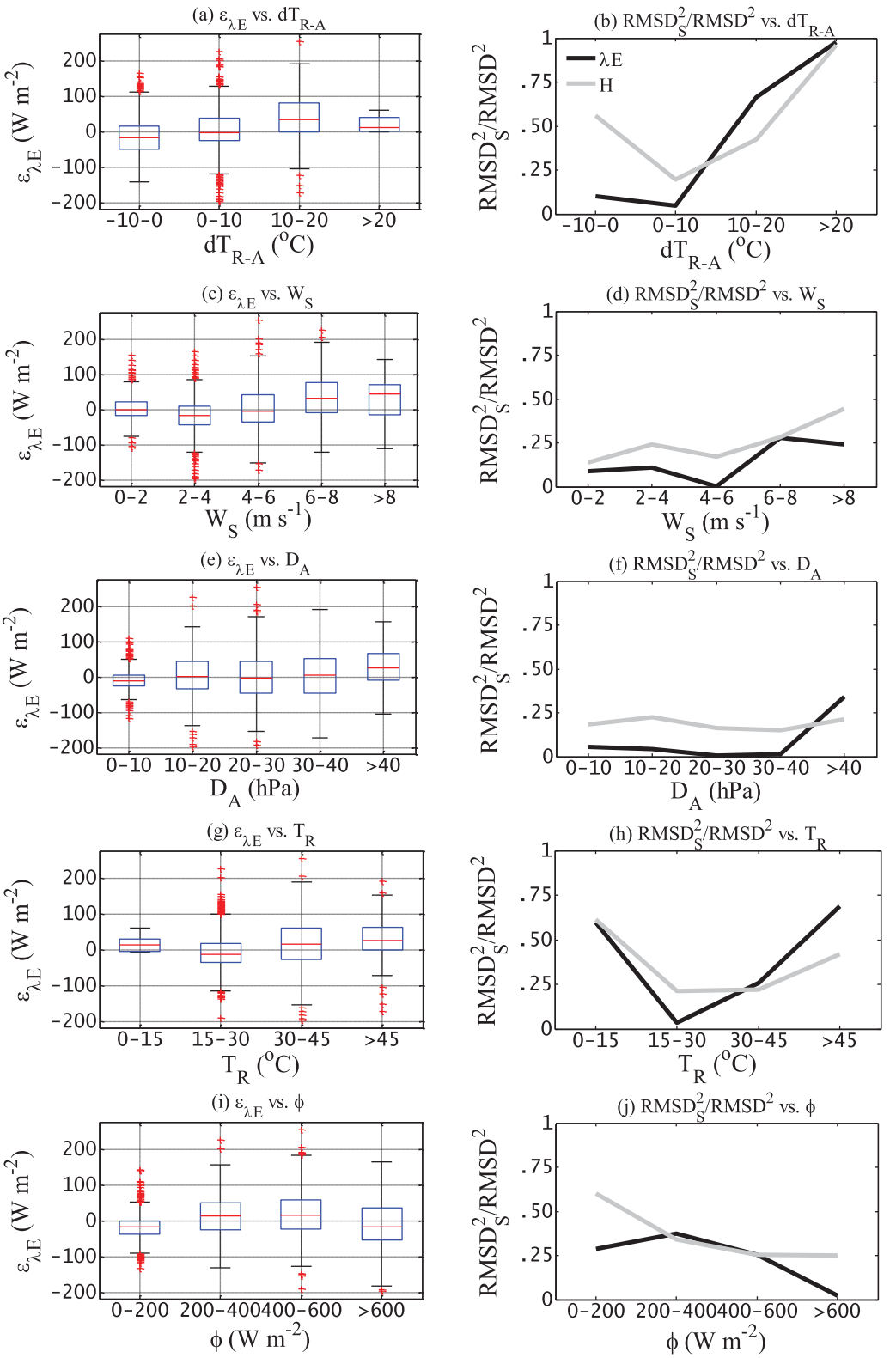

Figure 10. (a, c, e, g, and i) Box plots of statistical results showing the distribution of residual errors in STIC derived λE ($\varepsilon_{\lambda E}$) in relation to the environmental and land surface variables. The red line in box is the median $\varepsilon_{\lambda E}$, the lower part of the red line is the first quartile and upper part of the red line represents third quartile of $\varepsilon_{\lambda E}$. The residual error in *H* also follows the similar pattern but in opposite direction. (b, d, f, h, and j) Impact of the environmental and land surface variables on the ratio of the squares of systematic RMSD to total RMSD. The ratio is in fraction (ratio of 1 signifies 100%).

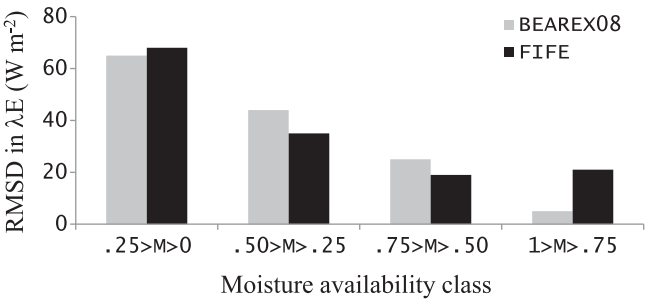

Figure 11. Pattern of λE RMSD according to different levels of surface moisture availability (M). This illustrates that the majority of the RMSD in λE is originated under substantial surface dryness conditions when M varies between 0 and 0.25.

per $\pm$ 1 K uncertainty in T_R) [*Mallick et al.*, 2015], and, therefore additional uncertainties expected from T_R induced through ϕ ($= R_N - G$) would be of minor importance.

Analysis of the surface energy fluxes obtained from STIC over a broad range of surface and atmospheric conditions showed that this approach can estimate λE within 71–96% of EC observations at half-hourly to hourly scale. Similarly the estimated H was within 62–85% of the EC observations (Figure 6). The origin of the discrepancies between modeled and measured H in SMEX02 and SAFARI2000 is unclear (Figures 6a, 6b, and 6f). Surface flux data obtained from the FIFE campaign were more vulnerable to errors because these fluxes are the average from 16 Bowen ratio flux stations and 6 EC towers [*Betts and Ball*, 1998]. In addition, the meteorological and radiation variables are the averages from many Portable Automatic Meteorological (PAM) stations and no attempts were made to account for land cover and terrain influence during the data averaging [*Betts and Ball*, 1998]. Therefore, the discrepancies between modeled and measured H in FIFE may be due to a combination of individual errors arising from data averaging of both the EC flux and AMS measurements. For BEAREX08, the larger errors in H (and λE also) (Figures 6c, 7e, and 7f) might have originated from ignoring the advection effects in the formulation of STIC or, more specifically due to excluding the role of wind speed in the scheme (which could be significant under high D_A). Large scale horizontal advection was dominant during BEAREX08 [*Alfieri et al.*, 2012; *Prueger et al.*, 2012] where parcels of irrigated cropland were in juxtaposition with hot and dry contrasting surface. This caused entrainment of dry and warm air from adjacent unirrigated fields, which increases the vapor pressure deficit (high evaporative demand) of the overlying air, resulting in large evaporative fluxes in excess of the net available energy over the irrigated fields [*Alfieri et al.*, 2012; *Prueger et al.*, 2012]. This led to very low values of H during midday, where heat was extracted from the dry air layer to drive the evaporation process. Under these conditions the potential evaporation (λE_P) is greater than the available energy (ϕ) and the advective energy is defined as $\Delta_A = \lambda E_P - \phi$ [*Prueger et al.*, 1996]. This advective energy is added to λE at the cost of reducing the sensible heat flux by the same amount [*Prueger et al.*, 1996]. Although the impact of advection was implicitly included in the final estimation of H, it was not sufficient to account for such anomalous conditions. This clearly points toward a need to better understand surface energy balance exchange for heterogeneous surfaces in arid and semiarid regions under conditions of strong local and regional advection. However, since the eddy covariance measurements of surface fluxes are not immune due to the effects of land surface heterogeneity [*Alfieri et al.*, 2012], uncertainties associated with the surface flux measurements will also impact the results to some extent.

The observed differences between the predicted fluxes by STIC and observations could partly be attributed to the different spatial representativeness of the T_R observations and flux measurements, which could not be accounted for by STIC. Since all the T_R measurements were conducted at 2 m above the surface, therefore the footprint size of T_R was also 2 m, whereas the EC surface flux observations generally has a footprint of 200–300 m upwind [*Norman et al.*, 2000]. Consequently, besides the requirement of simultaneous ground-based T_R and EC flux observations, the T_R measurements have to be calibrated using data that are more representative of the flux footprint area in order to obtain better agreement between predicted and observed surface fluxes [cf. *Norman et al.*, 2000]. The errors in the surface emissivity correction during the calibration of TIR instruments should also be reduced for improving the accuracy of the T_R measurements.

Marginal improvements in T_R based surface flux predictions over the SMEX02 (Figure 9) might be due to low surface to atmospheric water demand (and low thermal stress) during the limited study period and R_H based predictive fluxes are comparable to the T_R based surface fluxes. For the other experiments, although the R_H based method could reproduce the observed fluxes moderately well; however this method led to consistent overestimation under strong advection (as found in BEAREX08) as well as under high surface to

atmospheric water demand conditions (as found in SAFARI 2000 and FIFE) (Figure 9). An atmosphere with low D_A and high R_H indicates a moist humid atmosphere, but the underlying surface may be water stressed. R_H based M estimates will portray a wet surface condition for an otherwise dry surface, leading to λE being overestimated (H being underestimated). Similarly an atmosphere with high D_A and low R_H will portray a dry surface condition when actually it is wet, leading to λE being underestimated. Relatively low to moderate improvements in the λE and H estimates between T_R based hysteretic and nonhysteretic events (Figure 9) might be due to the occurrence of few hysteretic events during the experimental phase where λE was controlled by the stomata in the presence of both high D_A and water stress.

It is apparent that the residual errors at high W_S values became greater under increasing atmospheric moisture deficits, indicating that the effectiveness of wind increases with increasing D_A (Figures 10c and 10e). Increase in the residual errors at low to moderate values of W_S with high atmospheric moisture deficits can also be expected (as seen in BEAREX08) if wind is the only source of variation in the λE observations at high D_A. The data used in the present study do not cover the full growing season. There may be more frequent conditions having high W_S and high D_A later in the season under maximum vegetation cover conditions which may lead to additional λE (and H) errors. Relatively higher errors under high surface dryness (Figure 11) also highlighted the additional challenge in estimating λE using the PM model and its application to dry surfaces where T_R remains well above than that of the air temperature at the reference height. Under these conditions, the proper application of the PM equation requires iterative solution of T_0 via the energy balance so that the PM equation essentially decomposes back to its original energy and radiation balance components [*Allen*, 2013]. Relatively high RMSD in λE for low surface moisture availability range might also be attributed to expressing e_0^* at T_R, which suggests that the representation of e_0^* in STIC should be further developed. Estimating in-canopy vapor pressure deficit (or aerodynamic e_0 and e_0^*) might have an important effect for sparse vegetation or dry bare surfaces where both e_0 and e_0^* are influenced by a combination of conductance, net available energy, and surface moisture.

Although the performance of STIC in comparison to other TIR remote sensing based E modeling approaches cannot be directly assessed without independently evaluating STIC using remote sensing data, the error statistics obtained from the STIC approach can still be compared with other studies that earlier used in situ T_R measurements and tower meteorology for evaluating the surface energy fluxes in a single-source or two-source framework. Using hourly measurements of T_R, associated meteorological-micrometeorological variables and a two-source energy balance model (TSEB), *Anderson et al*. [2012] reported RMSD in daily λE and H of 1.5–1.8 MJ m^{-2} and 1.1–2.1 MJ m^{-2}, respectively, using the BEAREX08 data. *Kustas et al*. [2012] applied two different thermal E models (TSEB, Two-source Surface Energy Balance and DTD, Dual Temperature Difference) to a different data set from the same experiment and reported mean bias in H and λE to the order of -8 to -40 W m^{-2} and -18 to 31 W m^{-2}, respectively. Using the TSEB model, *Norman et al*. [1995] earlier reported MAPD in λE and H to the order of 17% and 32% using the FIFE experimental data. Using a single-source surface energy balance model (SEBS), *Su* [2002] reported RMSD of 61.34–82.79 W m^{-2} for λE and 28.61–36.19 W m^{-2} for H over semiarid shrub and grasses. STIC produced a relatively lower hourly and daily RMSD for both λE and H when applied to a variety of atmospheric turbulence conditions (from stable to strongly advective) as well as different land use types (see Table 2 and Figures 6, 7). However, the above studies used modeled R_N and G whereas STIC utilized all the input variables from in situ measurements. STIC has the advantage of being independent of any land surface parameterization to derive g_B and g_S that are typically required to model λE and H. The use of T_R and the temperature-saturation vapor pressure slopes to estimate the near surface moisture and vapor pressure (Figure A2) provided the information on lower boundary conditions for λE and H. The signal of surface roughness is also implicitly included in T_R (high roughness and dense vegetation will cause T_R to approach T_A), R_N (through albedo and surface emissivity), and G measurements that are direct inputs into STIC. Current results also indicate the efficiency of T_R information in capturing the temporal variability of surface fluxes within the PM framework in comparison to the methods that use relative humidity and D_A to constrain λE and H estimates [*Mallick et al*., 2013].

6. Conclusions

The analytical method presented in the framework of STIC demonstrated a physical integration of T_R into the PM equation to derive a "closure." STIC has the potential for simultaneously estimating surface energy

fluxes, conductances, and Priestley-Taylor parameter under limited surface-atmospheric conditions using the measurements of T_R, R_N, G, T_A, and R_H. These measurements are robust, simple to conduct, less expensive than EC or Bowen ratio measurements, and, therefore in many weather stations the inclusion of T_R and G sensors would be beneficial to obtain an estimate of the surface energy fluxes using the STIC methodology.

One of the novel aspects of STIC is the dynamic update of the Priestley-Taylor α through numerical iteration and determining α under limiting (or actual) environmental as well as surface ecohydrological conditions. This also makes STIC fluxes independent of the uncertainties associated in assigning α as a single parameter [*Mallick et al*., 2014].

Overall, the STIC is a self-contained approach, which does not require measured wind speed data and conductance parameterizations. Besides featuring logistical advantages over the parameterization based thermal surface energy balance models, the deviation from observations of λE and H are significantly lower. It should also be noted that although the case study described here provides general insights into thermal remote sensing of λE and H in the framework of the PM equation, these results may also to some extent be specific to the particular set of observational and land surface data used in this study. In other semiarid, arid, and hyper-arid landscapes, where moisture variability is more random and controlled by land-atmosphere-moisture interaction (particularly by relationships between R_N-T_R-D_A interaction and soil moisture), different results may potentially be obtained.

The most realistic and accurate description of evaporation from terrestrial vegetation is obtained by the PM equation, which is also considered as the ubiquitous equation for quantifying the response and feedback between vegetation and water cycle. This equation incorporates the combined effects of environmental, physical and ecophysiological variables on λE. While g_B describes the physical controls on evaporation containing information of atmospheric turbulence and vegetation roughness, g_S describes the ecophysiological controls of transpiration by the vegetation and is a compound of the leaf area index and the stomatal conductance. Changes in the vegetation dynamics, for instance, due to land use change, plant water stress and drought, are reflected in both the conductances because any change in the vegetation cover will alter the surface roughness, wind fields, leaf area, radiative interception and local micrometeorology. This will automatically lead to changes in the land-atmosphere interaction, evaporation-transpiration partitioning and associated heat fluxes; which will further make alterations in the cloud formation and precipitation [*Santanello et al*., 2013]. The accurate quantification of these changes requires surface energy flux estimation methods which are not conditional on the land surface parameterization. The STIC framework exploits the advection-aridity hypothesis and associated assumptions, but is independent of any exogenous semiempirical models for determination of complex turbulence and surface conductance and hence may be a valuable tool to quantify vegetation-water cycle interactions. Under the full vegetation cover conditions, the STIC framework can also be used to calculate the canopy conductance, thus creating a framework for comparing different g_S schemes within land surface models of varying complexity. However, under the partial vegetation cover conditions, λE derived through STIC needs to be partitioned into transpiration and evaporation to determine the stomatal conductance. This assumption needs to be tested further.

It is worth mentioning that there is further scope for improving the STIC methodology by incorporating the wind speed information and retrieving the aerodynamic vapor pressure (or within canopy vapor pressure deficit) at the level where the aerodynamic temperature (T_0) is retrieved. For the regional application of STIC using thermal remote sensing, M can also be derived in the framework of TVDI [*Sandholt et al*., 2002] or apparent thermal inertia (ATI) [*Verstraeten et al*., 2006] by exploiting the satellite derived T_R in conjunction with vegetation index and albedo, respectively. The ATI approach is already implemented to estimate M with higher accuracy [*Garcia et al*., 2013], rather than estimating M based on the complementary hypothesis of *Bouchet* [1963].

Exploring the feasibility of implementing STIC at larger spatial scale is an ongoing research topic. STIC needs measurements of T_A and R_H and for regional applications the accuracy of these two meteorological variables is very important. In addition, an uncertainty of 1 K in T_R appears to cause high errors in the conductance and surface fluxes, which implies that T_R has to be measured with an accuracy of at least 0.5 K. This requirement makes the application of this model challenging with satellite data notably over those areas where T_R retrieval errors are generally high due to inaccurate surface emissivity correction. The availability of Earth

observation data may provide an opportunity to extend the STIC methodology into the satellite platform by integrating the radiative flux information from Clouds and the Earth's Radiant Energy System (CERES) or Surface Radiation Budget (SRB), T_R and meteorological information from the Atmospheric Infrared Sounder (AIRS), Moderate Resolution Imaging Spectroradiometer (MODIS), Visible Infrared Imager Radiometer Suite (VIIRS) or future Sentinel-3 (dual view angle T_R from SLSTR, Sea and Land Surface Temperature Radiometer sensor), and soil moisture from the future Soil Moisture Active Passive (SMAP), thus allowing for more spatially explicit surface energy balance modeling and ecohydrological process studies.

Appendix A

A1. Advection-Aridity Hypothesis and Λ

To close the system of equations (in section 2) we need an expression for the evaporative fraction, Λ, which must include the dependence of Λ on the conductances. Therefore, we exploited two different representations of evaporation; the Penman (P) equation [*Penman*, 1948], and the Priestley-Taylor (PT) equation [*Priestley and Taylor*, 1972]. These two expressions are related to each other through the complementary relationship advection-aridity hypothesis [*Brutsaert and Stricker*, 1979] which is a modification of the original complementary hypothesis [*Bouchet*, 1963]. According to the complementary hypothesis, for a large homogeneous area of 1–10 km and away from sharp environmental discontinuities there exists a complementary feedback mechanism between potential evaporation (λE^*), evaporation (λE), and sensible heat flux (H) of the following form:

$$\lambda E + \lambda E^* = 2\lambda E_W \tag{A1}$$

λE^* is defined as the evaporation from a wet surface under the prevailing atmospheric condition, limited only by the amount of available energy. If moisture at the surface is unlimited (i.e., when $M = 1$), $\lambda E = \lambda E^*$ and this condition is referred to as the wet-environment evaporation (λE_W). Based on Bouchet's work, *Brutsaert and Stricker* [1979] proposed an advection-aridity hypothesis that allows the formulation of λE under nonpotential conditions. According to *Brutsaert and Stricker* [1979], λE_W was approximated as the potential evaporation according to *Priestley and Taylor* [1972], λE^*_{PT}, which represents the potential evaporation under the conditions of minimal advection and λE^* was approximated as the potential evaporation according to *Penman* [1948], λE^*_P, in order to capture the effects of large scale advection. Thus actual evapotranspiration could be computed by means of equation (A1) assuming $\lambda E^* = \lambda E^*_P$ and $\lambda E_W = \lambda E^*_{PT}$ [*Brutsaert and Stricker*, 1979; *Parlange and Katul*, 1992; *Ramirez et al*., 2005; *Huntington et al*., 2011].

$$\lambda E + \lambda E^*_P = 2\lambda E^*_{PT} \tag{A2}$$

This approach is independent of any submodel for representing the surface (or stomatal) conductance, soil moisture, or any other land surface measures of aridity. Taking advantage of this advection-aridity hypothesis we are able to express Λ in terms of the two conductances (g_B and g_S) and hence able to close the system of equations in the present scheme as described in section 2 [see also *Mallick et al*., 2014].

Although some theoretical arguments suggest partial fulfilment of the hypothesis of 1:1 compensation between λE and λE^* [*Lhomme*, 1997; *Sugita et al*., 2001], more recently *Ramirez et al*. [2005] found observational evidence for 1:1 compensation between λE and λE^*. We have also explored the potential complementary feedbacks between the atmosphere and the surrounding environment by relating high-temporal frequency λE^*_P and λE as a function of the surface moisture availability (M) following *Huntington et al*. [2011]. Figure A1a illustrates the complementary behavior between λE^*_P and λE; with quite scattered data points. However, an ideal complementarity could only be obtained by a normalizing λE^*_P and λE by λE_W [*Huntington et al*., 2011; *Kahler and Brutsaert*, 2006] as shown in Figure A1b, where a complementary relationship between λE^*_P and λE is clearly evident. However, during the winter months λE_W can be less that λE^*_P, which might inflate the $\lambda E^*_P/\lambda E_W$ ratio thus result in asymmetry in the complementary relationship [*Huntington et al*., 2011]

A2. Derivation of *M*

The retrieval of M is already described in *Mallick et al*. [2014] (as adopted from *Venturini et al*. [2008]). We hypothesize that the moisture availability at the surface and at the evaporating front are uniform and, therefore, M is derived from the surface-atmosphere information. According to *Noilhan and Planton* [1989], *Ye and Pielke* [1993], and *Boegh et al*. [2002], the transfer of λE from the surface can also be written as follows:

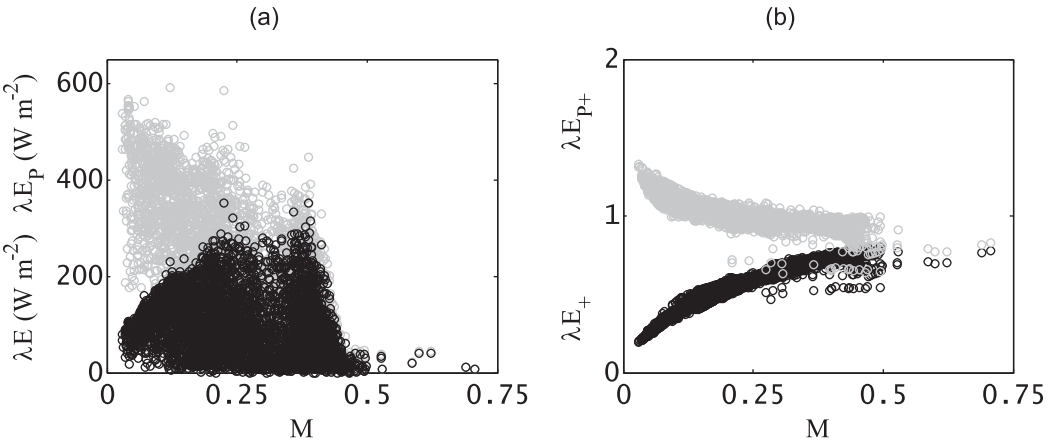

Figure A1. The (a) nonnormalized and (b) normalized complementary relationship between evapotranspiration (λE) (black circle), potential evaporation (λE_P) (gray circle), and wet environment evaporation (λE_w). The normalized λE_P (as λE_{P+}) (gray circle) was estimated as the ratio between λE_P and λE_w; whereas the normalized λE (as λE_+) (black circle) was estimated as the ratio between λE and λE_w according to *Kahler and Brutsaert* [2006].

$$\lambda E = \frac{\rho c_P}{\gamma} g_B (e_S - e_A) = M \lambda E^* = \frac{\rho c_P}{\gamma} M g_B \left(e_S^* - e_A\right) \tag{A3}$$

From equation (A3), a physical expression for M is given in terms of the temperature gradients.

$$M = \frac{(e_S - e_A)}{\left(e_S^* - e_A\right)} = \frac{s_1 (T_{SD} - T_D)}{s_2 (T_R - T_D)} \tag{A4}$$

where s_1 and s_2 are the slopes of the saturation vapor pressure and temperature between $(T_{SD} - T_D)$ versus $(e_S - e_A)$ and $(T_R - T_D)$ versus $(e_S^* - e_A)$ relationship. Figures A2a and A2b show the relationships between e_S, e_S^*, and e_A and their corresponding temperatures. By analogy to the dewpoint temperature, T_D, if the surface air is brought to saturation without affecting e_S then $e_S = f\{T_{SD}\}$. Thus, $T_{SD} < T_R$ for unsaturated surface and $T_{SD} \rightarrow T_R$ as the surface tends to saturation. For a dry surface $T_R \gg T_{SD}$, $e_S^* \gg e_S$, $(T_R - T_D) \gg (T_{SD} - T_D)$ and $M \rightarrow 0$. For a wet surface $e_S^* \cong e_S$, $T_R \cong T_{SD}$, $(T_R - T_D) \cong (T_{SD} - T_D)$ and $M \rightarrow 1$. When condensation occurs,

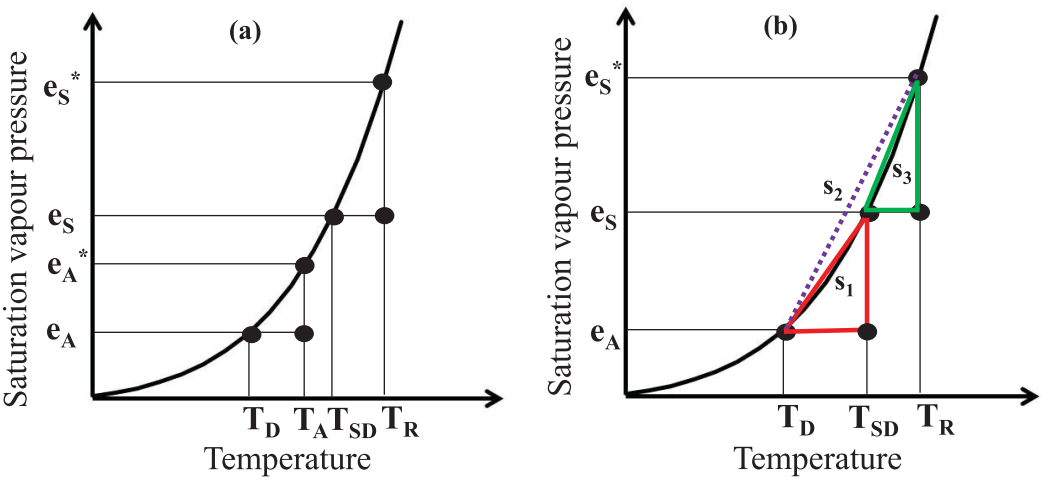

Figure A2. (a) Conceptual diagram of the saturation vapor pressure curve and the relationship among T_{SD}, T_R, e_S, and e_S^* in the context of surface at temperature T_R according to *Venturini et al*. [2008]. The air and dewpoint temperature of the overlying air is characterized by T_A and T_D with the vapor pressure e_A and e_A^*. Here T_{SD} is the surface dewpoint temperature, T_R is the radiometric surface temperature, e_S is the near surface vapor pressure, and e_S^* is the surface saturation vapor pressure. (b) Conceptual diagram of the linearized saturation vapor pressure curve to demonstrate the relationship between $(e_S - e_A)$ with $s_1(T_{SD} - T_D)$, $(e_S^* - e_S)$ with $s_3(T_R - T_{SD})$ and $(e_S^* - e_A)$ with $s_2(T_R - T_D)$. Here s_1, s_2, and s_3 are the slope of the saturation vapor pressure and temperature curve linearized according to *Monteith* [1965].

$T_R < T_A$ and $e_S < e_A$, otherwise e_S e_A and e_S ae_S^*. Hence, T_{SD} falls somewhere between T_R and T_D (Figure A2a) and can be computed by linearizing the saturation vapor pressure curve between the two levels (T_D, T_{SD}) and (T_{SD}, T_R) [*Monteith*, 1965].

Since T_R and e_A are available, s_2 can be calculated directly. However, when the differences in T_R and T_A are very large, the assumption of linearity of the saturation vapor pressure and temperature may produce errors [*Jackson et al*., 1981]. Therefore, in the present study the linearity is assumed till the difference between T_R and T_A is 5°C [*Jackson et al*., 1981] after which s_2 is approximated at T_R.

According to Figure A2,

$$s_1 = \frac{(e_S - e_A)}{(T_{SD} - T_D)} \tag{A5}$$

$$s_3 = \frac{(e_S^* - e_S)}{(T_R - T_{SD})} \tag{A6}$$

Combining equations (A5) and (A6), an expression of T_{SD} can be obtained.

$$T_{SD} = \frac{(e_S^* - e_A) - s_3 T_R + s_1 T_D}{(s_1 - s_3)} \tag{A7}$$

Here we have one equation (A7) and two unknowns (s_1 and s_3), which is not uniquely solvable using the assumptions and the iterative procedure described in *Venturini et al*. [2008] as adopted by *Mallick et al*. [2014]. However, in a more recent follow up study, *Venturini et al*. [2012] proposed a simplified method of T_{SD} estimation. Following *Venturini et al*. [2012], we similarly revise some aspects of T_{SD} estimation in the present analysis, by directly assigning s_3 as a function of T_R and s_1 as a function of T_D, the general form of which is $\left[s = 4098 \frac{6.108 e^{\frac{17.27T}{(T+237.3)}}}{(T+237.3)^2}\right]$. According to Figure A2b, T_R and T_D are the two end member temperatures of the saturation vapor pressure-temperature curve. Under extremely dry surface conditions $T_{SD} \rightarrow T_D$, while under extremely wet conditions $T_{SD} \rightarrow T_R$. Therefore, T_{SD} at any point of time is a blend of these two end member temperatures (T_R and T_D) depending on the degree of surface dryness/wetness, atmospheric humidity, and surface-atmospheric coupling. Considering different sets of surface-atmospheric dryness/wetness conditions, the following situations may occur:

1. Surface and atmosphere both are extremely dry: This implies a strong surface-atmosphere coupling, typical conditions found in dry-tropical, arid, semiarid, hyper-arid, savanna, and Mediterranean climates. Here T_R is extremely high and T_D is very low (because of low atmospheric humidity). Under such conditions T_{SD} will be very close to T_D and the difference between T_R and T_{SD} will be very large. Assigning s_1 in T_D and s_3 in T_R will reasonably constrain equation (A7) because s_3 (actual) $\gg$ s_1 (actual) in such circumstances and s_3 (T_R) (virtual) will also be significantly higher than s_1 (T_D) (virtual) under such conditions.
2. Surface and atmosphere both are wet: This implies a weak surface-atmosphere coupling, typical conditions found in wet tropical and wet temperate regions or during rainy seasons. Here T_R is substantially low, T_D is reasonably high (because of high atmospheric humidity), leading to very low $T_R - T_D$. Under such conditions T_{SD} will be very close to T_R because of high surface humidity and the difference between T_R and T_{SD} will be very small. Therefore, assigning s_1 in T_D and s_3 in T_R will again reasonably constrain equation (A7) because s_3 (actual) will be close to s_1 (actual) in such circumstances and s_3 (T_R) (virtual) will also be close to s_1 (T_D) (virtual).
3. Surface is dry and atmosphere is moist: This implies moderate surface-atmosphere coupling, typical conditions found in tropical monsoon climate before the onset of rainfall when water vapor in the atmosphere increases but surface remains dry due to no rainfall. Arid and semiarid areas close to the sea (e.g., Mediterranean) with high atmospheric water vapor and dry soil conditions also belong to this category. Here T_R is moderate to high, T_D is high due to the high atmospheric water vapor and $T_R - T_D$ is moderate to low. Under such conditions the magnitude of $T_R - T_{SD}$ will be high (because of high surface dryness). Therefore, assigning s_1 in T_D and s_3 in T_R will also reasonably constrain equation (A7) because s_3 (actual) will be bigger than s_1 (actual) in such circumstances and s_3 (T_R) (virtual) will also be larger than s_1 (T_D) (virtual).

In order to support the above assumptions, the following analysis has been carried out.

Table A1. Error Analysis of Modeled T_{SD} and M Estimates in Comparison to Synthetic T_{SD} and M From MERRA

	Correlation Coefficient (r) in T_{SD} and M in Variable Dry-Wet Spatial Domain		
Variable	Dry (North-Central Africa)	Intermediate (North America)	Wet (Amazon Basin)
T_{SD}	0.76 ($p = 0.00$)	0.46 ($p = 0.01$)	0.97 ($p = 0.00$)
M	0.68 ($p = 0.00$)	0.16 ($p = 0.02$)	0.58 ($p = 0.00$)

A3. Evaluating M at Landscape and Feld Scale

Taking monthly MERRA (Modern Era Retrospective-analysis for Research and Applications) data, we have estimated T_{SD} and M following the same procedure as described in the manuscript and compared these estimates against the simulated T_{SD} and M as available in the MERRA database. Here we treat MERRA as a synthetic data set and the 1:1 scatterplot between modeled versus synthetic T_{SD} and M are shown in Figures A3a and A3b for three different soil water availability classes (wet, intermediate, and dry). These classes represent 10 × 10 gridded data points over the Amazon Basin (wet), North-central Africa (dry), and North America (intermediate). This shows relatively good correspondence between the modeled versus synthetic T_{SD} and M. The correlation between modeled and synthetic T_{SD} was in the range of 0.46–0.97 ($p < 0.05$) (Table A1),

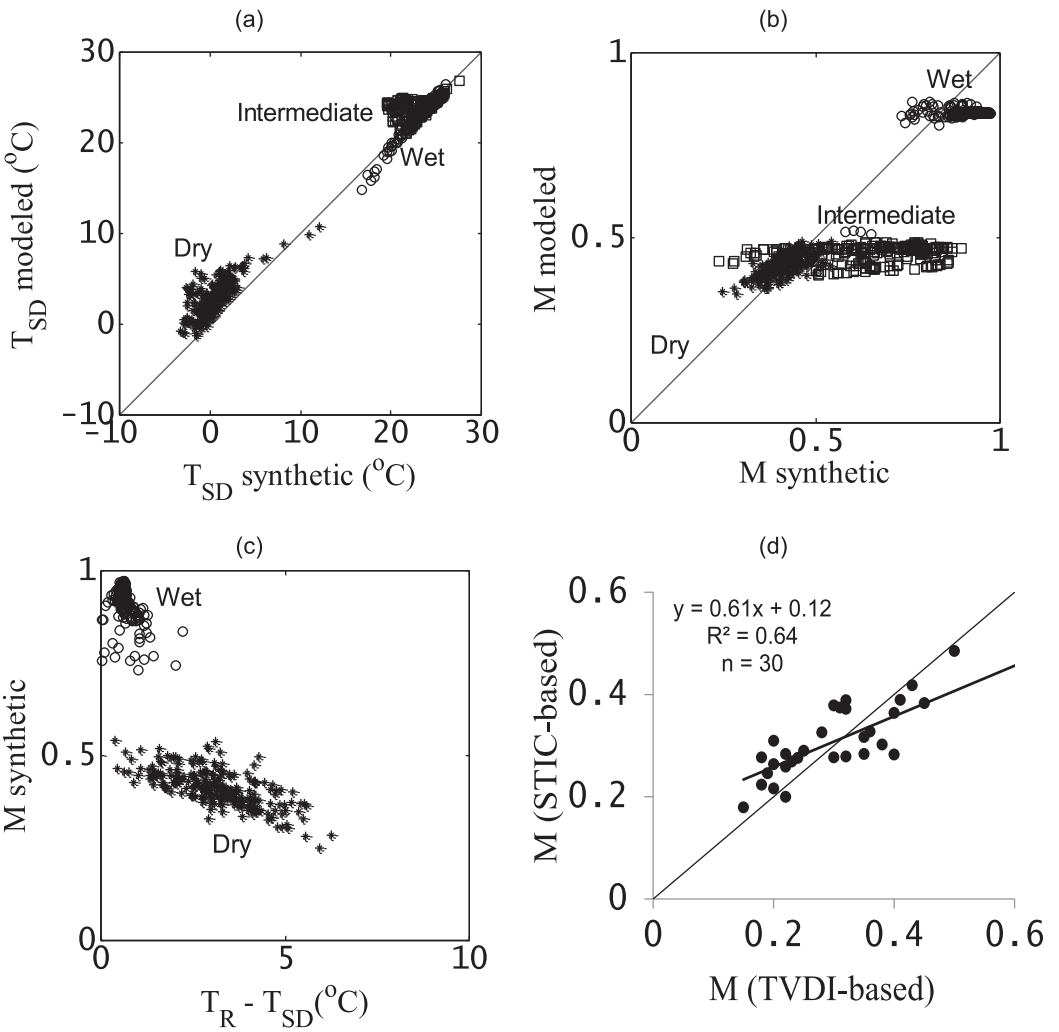

Figure A3. (a) Comparison between modeled and synthetic T_{SD} over a broad range of surface wetness class. (b) Comparison between modeled and synthetic M over a broad range of surface wetness class. (c) Two-dimensional scatter between synthetic M and $T_R - T_{SD}$ difference. This shows the $T_{SD} \rightarrow T_R$ with an increase in surface moisture and the difference between them become large with an increase in surface dryness. (d) Comparison of STIC derived M with TVDI derived M over Indian agroecosystems. The round markers indicate the data of wet landscapes, square markers indicates the data over intermediately wet-dry landscapes, and star markers indicate the data over over dry landscapes.

whereas for M the correlation varied from 0.16 to 0.68 ($p < 0.05$) for the three broad soil water availability subclasses (Table A1). Given T_D is the lower most temperature limit and T_{SD} will be very low under dry conditions ($T_{SD} \rightarrow T_D$), we expect the difference of ($T_R - T_{SD}$) to be bigger for the dry cases and the differences to be small for the wet cases. Figure A3c also depicts the similar behavior and this further proves the robustness of the assumptions made in the current M estimation method. From this comparison it appears that although the simplified M retrieval method performed substantially good at capturing the general wetness patterns for the two extreme climatic categories (wet, dry) along the 1:1 line, it is not capable of capturing the wetness variations within the intermediate dry-wet climatic region (Figure A3b). However, these results are based on the synthetic data and any error in the MERRA data simulation of M, T_R, T_D, and T_{SD} will affect this evaluation.

We have also compared the M estimation method by comparing the STIC based M estimates (M_STIC) against TVDI (Temperature Vegetation Dryness Index) [*Sandholt et al*., 2002] derived M estimates (M_TVDI) by using the data of *Mallick et al*. [2009] over different agroecosystems in India (Figure A3d). For more detail about the data and agroecosystems, see *Mallick et al*. [2009]. This also shows reasonably good correspondence where M_STIC could explain 64% variability of M_TVDI and the RMSD between the two wetness estimates were 0.07. These two case studies seemingly depict the validity of the assumptions used for estimating M in the current manuscript. However, a detailed study is further needed for assessing the impact of different M retrieval methodologies on the error propagation in λE and H estimates. It is important to mention that the saturation vapor pressure (SVP) concept assumes a free pure water surface, where the forces holding the water molecules to the surface are the bonds between the nearest molecules. These bonds are broken by the thermal energy to produce the evaporation [*Venturini et al*., 2008]. But for an unsaturated surface, where multiple forces hold the water to the soil vegetation interface, more thermal energy would be required to vaporize the soil-vegetation water molecules [*Venturini et al*., 2008]. Therefore, vapor pressure (e_0 and e_s) for an unsaturated surface would be smaller than that derived from a SVP curve. This is the reason that e_0 estimation was based on M and not on T_{SD}.

Acknowledgments

The SMEX02 data for this paper are available at National Snow and Ice Data Centre (NSIDC), University of Colorado, Boulder (http://nsidc.org/data/amsr_validation/soil_moisture/smex02/) (Data set name: Meteorological, SMEX02 SMACEX Tower Meteorological/Flux Data: Iowa). The SAFARI data are available through Oak Ridge National Laboratory Distributed Active Archive Center (ftp://daac.ornl.gov/data/safari2k), Oak Ridge, Tennessee, US. FIFE data sets are available from Alan Betts (through http://alanbetts.com/research/). MERRA data are available through http://disc.sci.gsfc.nasa.gov/daac-bin/DataHoldings.pl. The TVDI data of *Mallick et al*. [2009] was a part of the project "Energy Water Balance Monitoring from Geostationary Platform for Agricultural Applications" funded by Space Applications Centre, ISRO. The research was conducted at the Luxembourg Institute of Science and Technology (previously Centre de Recherché Public- Gabriel Lippmann) under internally funded REMOD project. K.M. and A.J. was earlier supported by NERC grant (NEE0191531) during the initial development of the work. All the copyrights of 2015 are reserved. The authors declare no conflict of interest. USDA is an equal opportunity provider and employer.

Appendix B

B1. Modification of PMBL

A modification of the original PMBL [*Mallick et al*., 2013] is performed to make the structure of PMBL identical to STIC but having R_H (and D_A) as main variables for estimating M and constraining the conductances. In the modified method, an initial estimate of the conductances, T_0, Λ, and λE are obtained by assigning $M = 1$ and e_0 as saturation vapor pressure at T_A. From the initial T_0, initial e_0^*, s_3, and T_{SD} (according to equation (A7)) were estimated. The process is then iterated by simultaneously updating M (from the initial estimates of T_0, s_3, and T_{SD} using equation (A4)), e_0 (according to equation (23)), conductances, T_0, and Λ until a stable value of λE is achieved. Repeating this process produces stable value of λE within 10–12 iterations.

References

Alfieri, J. G., W. P. Kustas, J. H. Prueger, L. E. Hipps, J. L. Chavez, A. N. French, and S. R. Evett (2011), Intercomparison of nine micrometeorological stations during the BEAREX08 field campaign, *J. Atmos. Oceanic Technol.*, *28*, 1390–1406.

Alfieri, J. G., et al. (2012), On the discrepancy between eddy covariance and lysimetry-based surface flux measurements under strongly advective conditions, *Adv. Water Res.*, *50*, 62–78.

Allen, R. G. (2013), How John Monteith's formulation of the Penman-Monteith equation helped to standardize the world of reference evapotranspiration, paper presented at Water, Food, energy & Innovation for a Sustainable World, American Society of Agronomy (ASA), Crop Science Society of America (CSSA) & Soil Science Society of America (SSSA) International Annual Meetings, Tampa, Fla, 3–6 Nov.

Anderson, M. C., J. M. Norman, G. R. Diak, W. P. Kustas, and J. R. Mecikalski (1997), A two-source time-integrated model for estimating surface fluxes using thermal infrared remote sensing, *Remote Sens. Environ.*, *60*, 195–216.

Anderson, M. C., J. M. Norman, J. R. Mecikalski, J. A. Otkin, and W. P. Kustas (2007), A climatological study of evapotranspiration and moisture stress across the continental United States based on thermal remote sensing. 1: Model formulation, *J. Geophys. Res.*, *112*, D10117, doi:10.1029/2006JD007506.

Anderson, M. C., J. M. Norman, W. P. Kustas, R. Houborg, P. J. Starks, and N. Agam (2008), A thermal-based remote sensing technique for routine mapping of land-surface carbon, water and energy fluxes from field to regional scales, *Remote Sens. Environ.*, *112*, 4227–4241.

Anderson, M. C., et al. (2012), Mapping daily evapotranspiration at Landsat spatial scales during the BEAREX'08 field campaign, *Adv. Water Res.*, *50*, 162–177.

Baldocchi, D. D., R. J. Luxmoore, and J. R. Hatfield (1991), Discerning the forest from the trees: An essay on scaling canopy stomatal conductance, *Agric. For. Meteorol.*, *54*(2–4), 197–226.

Baldocchi, D. D., et al. (2001), Fluxnet: A new tool to study the temporal and spatial variability of ecosystem-scale carbon dioxide, water vapor, and energy flux densities, *Bull. Am. Meteorol. Soc.*, *82*(11), 2415–3434.

Ball, J. T., I. E. Woodrow, and J. A. Berry (1987), A model predicting stomatal conductance and its contribution to the control of photosynthesis under different environmental conditions, in *Progress in Photosynthesis Research*, vol. 4, edited by J. Biggins and M. Nijhoff, pp. 5.221–5.224, Martinus Nijhoff, Dordrecht, Netherlands.

Bastiaansssen, W. G. M., M. Menenti, R. A., Feddes, and A. A. M. Holtslag (1998), A remote sensing surface energy balance algorithm for land (SEBAL). 1: Formulation, *J. Hydrol.*, *212–213*, 198–212.

Betts, A. K., and J. H. Ball (1998), FIFE surface climate and site-average data set 1987–1989, *J. Atmos. Sci.*, *55*, 1091–1108.

Beven, K. (1979), A sensitivity analysis of the Penman-Monteith actual evapotranspiration estimates, *J. Hydrol.*, *44*(3–4), 169–190.

Blonquist, J. M., J. M. Norman, and B. Bugbee (2009), Automated measurement of canopy stomatal conductance based on infrared temperature, *Agric. For. Meteorol.*, *149*, 1931–1945.

Boegh, E., and H. Soegaard (2004), Remote sensing based estimation of evapotranspiration rates, *Int. J. Remote Sens.*, *25*(13), 2535–2551.

Boegh, E., H. Soegaard, N. Hannan, P. Kabat, and L. Lesch (1999), A remote sensing study of the NDVI-TS relationship and the transpiration from sparse vegetation in the Sahel based on high-resolution satellite data, *Remote Sens. Environ.*, *96*, 224–240.

Boegh, E., H. Soegaard, and A. Thomsen (2002), Evaluating evapotranspiration rates and surface conditions using Landsat TM to estimate atmospheric resistance and surface resistance, *Remote Sens. Environ.*, *79*, 329–343.

Bouchet, R. J. (1963), Evapotranspiration réelle et potentielle, signification climatique, *Int. Assoc. Sci. Hydrol.*, 62, 134–142.

Bowen, I. S. (1926), The ratio of heat losses by conduction and by evaporation from any water surface, *Phys. Rev.*, *27*, 779–787.

Brutsaert, W., and H. Stricker (1979), An advection-aridity approach to estimate actual regional evapotranspiration, *Water Resour. Res.*, *15*(2), 443–450.

Buck, A. L. (1981), New equations for computing vapor pressure and enhancement factor, *J. Appl. Meteorol.*, *20*, 1527–1532.

Campbell, G. S., and J. M. Norman (1998), *An Introduction to Environmental Biophysics*, Springer, New York.

Chavez, J. L., C. M. U. Neale, L. E. Hipps, J. H. Prueger, and W. P. Kustas (2005), Comparing aircraft-based remotely sensed energy balance fluxes with eddy covariance tower data using heat flux source area functions, *J. Hydrometeorol.*, *6*, 923–940.

Cleugh, H. A., R. Leuning, Q. Mu, and S. W. Running (2007), Regional evaporation estimates from flux tower and MODIS satellite data, *Remote Sens. Environ.*, *106*, 285–304.

Colaizzi, P. D., et al. (2012), Two-source energy balance model estimates of evapotranspiration using component and composite surface temperatures, *Adv. Water Res.*, *50*, 134–151.

Dewar, R. C. (1995), Interpretation of an empirical model for stomatal conductance in terms of guard cell function, *Plant Cell Environ.*, *18*(4), 365–372.

Ershadi, A., M. F. McCabe, J. P. Evans, N. W. Chaney, and E. F. Wood (2014), Multi-site evaluation of terrestrial evaporation models using FLUXNET data, *Agric. For. Meteorol.*, *187*, 46–61.

Evett, S. R., W. P. Kustas, P. H. Gowda, M. C. Anderson, J. H. Prueger, and T. A. Howell (2012), Overview of the Bushland evapotranspiration and agricultural remote sensing experiment 2008 (BEAREX08): A field experiment evaluating methods for quantifying ET at multiple scales, *Adv. Water Res.*, *50*, 4–19.

Garcia, M., I. Sandholt, P. Ceccato, M. Ridler, E. Mougin, L. Kergoat, L. Morillas, F. Timouk, R. Fensholt, and F. Domingo (2013), Actual evapotranspiration in drylands derived from in-situ and satellite data: Assessing biophysical constraints, *Remote Sens. Environ.*, *131*, 103–118.

Granger, R. J., and D. M. Gray (1989), Evaporation from natural nonsaturated surfaces, *J. Hydrol.*, *111*, 21–29.

Hall, F. G., K. F. Huemmrich, S. J. Goetz, P. J. Sellers and J. E. Nickeson (1992), Satellite remote sensing of surface energy balance: Success, failures and unresolved issues in FIFE, *J. Geophys. Res.*, *97*(D17), 19,061–19,089.

Huband, N. D. S., and J. L. Monteith (1986), Radiative surface temperature and energy balance of a wheat canopy. I: Comparison of radiative and aerodynamic canopy temperature, *Boundary Layer Meteorol.*, *36*, 1–17.

Huntington, J. L., J. Szilagyi, S. Tyler, and G. Pohll (2011), Evaluating the complementary relationship for estimating evapotranspiration from arid shrublands, *Water Resour. Res.*, *47*, W05533, doi:10.1029/2010WR009874.

Jackson, R. D., S. B. Idso, R. J. Reginato, and P. J. Pinter Jr. (1981), Canopy temperature as a crop water stress indicator, *Water Resour. Res.*, *17*(4), 1133–1138.

Jarvis, P. G. (1976), The interpretation of leaf water potential and stomatal conductance found in canopies in the field, *Philos. Trans. R. Soc. London B*, *273*, 593–610.

Kahler, D. M., and W. Brutsaert (2006), Complementary relationship between daily evaporation in the environment and pan evaporation, *Water Resour. Res.*, *42*, W05413, doi:10.1029/2005WR004541.

Kanemasu, E. T., et al. (1992), Surface flux measurements in FIFE: An overview, *J. Geophys. Res.*, *97*(D17), 18,547–18,556.

Katul, G. G., S. Manzoni, S. Palmroth, and R. Oren (2010), A stomatal optimization theory to describe the effects of atmospheric CO_2 on leaf photosynthesis and transpiration, *Ann. Bot.*, *105*(3), 431–442.

Kustas, W. P., and M. C. Anderson (2009), Advances in thermal infrared remote sensing for land surface modeling, *Agric. For. Meteorol.*, *149*, 2071–2081.

Kustas, W. P., and J. M. Norman (1999), Evaluation of soil and vegetation heat flux predictions using simple two-source model with radiometric temperature for partial canopy cover, *Agric. For. Meteorol.*, *94*, 13–29.

Kustas, W. P., J. L. Hatfield, and J. H. Prueger (2005), The Soil Moisture-Atmosphere Coupling Experiment (SMACEX): Background, hydrometeorological conditions, and preliminary findings, *J. Hydrometeorol.*, *6*, 791–804.

Kustas, W. P., et al. (2012), Evaluating the two-source energy balance model using local thermal and surface flux observations in a strongly advective irrigated agricultural area, *Adv. Water Res.*, *50*, 120–133.

Lascano, R. J., and C. H. M. van Bavel (2007), Explicit and recursive calculation of potential and actual evapotranspiration, *Agron. J.*, *99*, 585–590.

Lee, T. J., and R. Pielke (1992), Estimating the soil surface specific humidity, *J. Appl. Meteorol.*, *31*, 480–484.

Leuning, R. (1995), A critical appraisal of a combined stomatal—Photosynthesis model for c3 plants, *Plant Cell Environ.*, *18*, 339–355.

Lhomme, J. P. (1997), A theoretical basis for the Priestley-Taylor coefficient, *Boundary Layer Meteorol.*, *82*, 179–191.

Lhomme, J. P., and C. Montes (2014), Generalized combination equations for canopy evaporation under dry and wet conditions, *Hydrol. Earth Systems Sci.*, *18*, 1137–1149.

Lhomme, J. P., A. Chehbouni, and B. Monteny (2000), Sensible heat flux-radiometric surface temperature relationship over sparse vegetation: Parameterizing B-1, *Boundary Layer Meteorol.*, *97*(3), 431–457.

Liu, S., L. Lu, D. Mao and L. Jia (2007), Evaluating parameterizations of aerodynamic resistance to heat transfer using field measurements, *Hydrol. Earth Syst. Sci.*, *11*, 769–783.

Mallick, K., B. K. Bhattacharya, and N. K. Patel (2009), Estimating volumetric surface moisture content for cropped soils using a soil wetness index based on surface temperature and NDVI, *Agric. For. Meteorol.*, *149*(8), 1327–1342.

Mallick, K., A. J. Jarvis, J. B. Fisher, K. P. Tu, E. Boegh and D. Niyogi (2013), Latent heat flux and canopy conductance based on Penman-Monteith and Bouchet's complementary hypothesis, *J. Hydrometeorol.*, *14*, 419–442.

Mallick, K., et al. (2014), A surface temperature initiated closure (STIC) for surface energy balance fluxes, *Remote Sens. Environ.*, *141*, 243–261.

Mallick, K., et al. (2015), Components of near-surface energy balance derived from satellite soundings—Part 1: Noontime net available energy, *Biogeosciences*, *12*, 433–451.
Manzoni, S., G. Vico, S. Palmroth, A. Porporato, and G. Katul (2013), Optimization of stomatal conductance for maximum carbon gain under dynamic soil moisture, *Adv. Water Res.*, *62*, 90–105.
Monteith, J. L. (1965), Evaporation and environment, in *Symposium of the Society for Experimental Biology, The State and Movement of Water in Living Organisms*, vol. 19, edited by G. E. Fogg, pp. 205–234. Academic, N. Y.
Monteith, J. L. (1981), Evaporation and surface temperature, *Q. J. R. Meterol. Soc.*, *107*, 1–27.
Monteith, J. L. (1995), Accommodation between transpiring vegetation and the convective boundary layer, *J. Hydrol.*, *166*, 251–263.
Mu, Q., F. A. Heinsch, M. Zhao, and S. W. Running (2007), Development of a global evapotranspiration algorithm based on MODIS and global meteorology data, *Remote Sens. Environ.*, *111*, 519–536.
Mu, Q., M. Zhao, and S. W. Running (2011), Improvements to a MODIS global terrestrial evapotranspiration algorithm, *Remote Sens. Environ.*, *115*, 1781–1800.
Noilhan, J., and S. Planton (1989), A simple parameterization of land surface processes for meteorological models, *Mon. Weather Rev.*, *117*, 536–549.
Norman, J. M., W. P. Kustas, and K. S. Humes (1995), A two-source approach for estimating soil and vegetation energy fluxes in observations of directional radiometric surface temperature, *Agric. For. Meteorol.*, *77*, 263–293.
Norman, J. M., W. P. Kustas, J. H. Prueger, and G. R. Diak (2000), Surface flux estimation using radiometric temperature: A dual-temperature-difference method to minimize measurement errors, *Water Resour. Res.*, *36*(8), 2263−−2274.
Parlange, M. B., and G. G. Katul (1992), An advection-aridity evaporation model, *Water Resour. Res.*, *28*(1), 127–132.
Penman, H. L. (1948), Natural evaporation from open water, bare soil, and grass, *Proc. R. Soc. London, Ser. A*, *193*, 120–146.
Pereira, A. R. (2004), The Priestley-Taylor parameter and the decoupling factor for estimating reference evapotranspiration, *Agric. For. Meteorol.*, *125*, 305–313.
Priestley, C. H. B., and R. J. Taylor (1972), On the assessment of surface heat flux and evaporation using large scale parameters, *Mon. Weather Rev.*, *100*, 81–92.
Prueger, J. H., L. E. Hipps, and D. I. Cooper (1996), Evaporation and the development of the local boundary layer over an irrigated surface in an arid region, *Agric. For. Meteorol.*, *78*, 223–237.
Prueger, J. H., J. G. Alfieri, and L. E. Hipps (2012), Patch scale turbulence over dryland and irrigated surfaces in a semi-arid landscape under advective conditions during BEAREX08, *Adv. Water Res.*, *50*, 106–119.
Ramirez, J. A., M. T. Hobbins, and T. C. Brown (2005), Observational evidence of the complementary relationship in regional evaporation lends strong support for Bouchet's hypothesis, *Geophys. Res. Lett.*, *32*, L15401, doi:10.1029/2005GL023549.
Raupach, M. R., and J. J. Finnigan (1995), Scale issues in boundary-layer meteorology: Surface energy balance in heterogeneous terrain, *Hydrol. Processes*, *9*, 589–612.
Sandholt, I., K. Rasmussen, and J. Andersen (2002), A simple interpretation of the surface temperature/vegetation index space for assessment of surface moisture status, *Remote Sens. Environ.*, *79*, 213–224.
Santanello, J., C. D. Peters-Lidard, A. Kennedy, S. V. Kumar, and S. Zhou (2013), Diagnosing the nature of land–atmosphere coupling: A case study of dry/wet extremes in the U.S. Southern Great Plains, *J. Hydrometeorol.*, *14*(1), 3–24, doi:10.1175/JHM-D-12–023.1.
Scholes, R. J., et al. (2002), Trends in savanna structure and composition on an aridity gradient, *J. Veg. Sci.*, *13*, 419–428.
Segal, M., X. Jia, Z. Ye, and R. A. Pielke (1990), On the effect of daytime surface evaporation on pollution dispersion, *Atmos. Environ., Part A*, *24*(7), 1801–1811.
Sellers, P. J., F. G. Hall, G. Asrar, D. E. Strebel, and R. E. Murphy (1992), An overview of the First International Satellite Land Surface Climatology Project (ISLSCP) Field Experiment (FIFE), *J. Geophys. Res.*, *97*(D17), 18,345–18,371.
Shuttleworth, W. J., R. J. Gurney, A. Y. Hsu, and J. P. Ormsby (1989), FIFE: The variation in energy partition at surface flux sites, in *Remote Sensing and Large Scale Processes*, *Proceedings of the IAHS Third International Assembly*, vol. 186, edited by A. Rango, pp. 67–74, IAHS Publ., Baltimore, Md.
Su, Z. (2002), The surface energy balance system (SEBS) for estimation of turbulent heat fluxes, *Hydrol. Earth Syst. Sci.*, *61*(1), 85–99.
Sugita, M., J. Usui, I. Tamagawa, and I. Kaihotsu (2001), Complementary relationship with convective boundary layer model to estimate regional evaporation, *Water Resour. Res.*, *37*(2), 353–365.
Troufleau, D., J. P. Lhomme, B. Monteny, and A. Vidal (1997), Sensible heat flux and radiometric surface temperature over sparse Sahelian vegetation. I: An experimental analysis of kB^{-1} parameter, *J. Hydrol.*, *188–189*, 815–838.
van der Kwast, J., W. Timmermans, A. Gieske, Z. Su, A. Olioso, L. Jia, J. Elbers, D. Karssenberg and S. de Jong (2009), Evaluation of the Surface Energy Balance System (SEBS) applied to ASTER imagery with flux-measurements at the SPARC 2004 site (Barrax, Spain), *Hydrol. Earth Syst. Sci.*, *13*, 1337–1347.
van der Tol, C., S. van der Tol, A. Verhoef, B. Su, J. Timmermans, C. Houldcroft and A. Gieske (2009), A Bayesian approach to estimate sensible and latent heat over vegetated land surface, *Hydrol. Earth Syst. Sci.*, *13*, 749–758.
Venturini, V., S. Islam, and L. Rodriguez (2008), Estimation of evaporative fraction and evapotranspiration from MODIS products using a complementary based model, *Remote Sens. Environ.*, *112*(1), 132–141.
Venturini, V., C. Krepper, and L. Rodriguez (2012), Evapotranspiration estimation based on the complementary relationships, in *Evapotranspiration—Remote Sensing and Modeling*, edited by A. Irmak, 526 pp., InTech, Nebr., doi:10.5772/725.
Verstraeten, W. W., F. Veroustraete, C. J. van der Sande, I. Grootaers, and J. Feyen (2006), Soil moisture retrieval using thermal inertia, determined with visible and thermal spaceborne data validated for European forests, *Remote Sens. Environ.*, *101*, 299–314.
Willmott, C. J. (1982), Some comments on the evaluation of model performance, *Bull. Am. Meteorol. Soc.*, *63*, 1309–1313.
Ye, Z., and R. Pielke (1993), Atmospheric parameterization of evaporation from non-plant-covered surfaces, *J. Appl. Meteorol.*, *32*, 1248–1258.
Zhang, Q., S. Manzoni, G. Katul, A. Porporato, and D. Yang (2014), The hysteretic evapotranspiration-vapor pressure deficit relation, *J. Geophys. Res. Biogeosci.*, *119*, 125–140, doi:10.1002/2013JG002484.
Zheng, H., Q. Wang, X. Zhu, Y. Li, and G. Yu (2014), Hysteresis responses of evapotranspiration to meteorological factors at a diel timescale: Patterns and causes, *PLOS One*, *9*(6), e98857, doi:10.1371/journal.pone.0098857.g008.

Erratum

In the originally published article, the author name for the reference and citations "Collaizi et al, 2012" should have appeared as "Colaizzi et al., 2012." In Table 2, in the "Biome Type" column, row 2 should appear as "Agroecosystem (cotton)" instead of "Agroecosystem (corn and soybean)." This article may be considered the authoritative version of record.